Transverse optical instability patterns in semiconductor microcavities: Polariton scattering and low-intensity all-optical switching

M. H. Luk,[1] Y. C. Tse,[1] N. H. Kwong,[1,2,3,*] P. T. Leung,[1] Przemyslaw Lewandowski,[4] R. Binder,[3,5] and Stefan Schumacher[4]

[1]*Department of Physics and Institute of Theoretical Physics, The Chinese University of Hong Kong, Hong Kong SAR, China*

[2]*Center of Optical Sciences, The Chinese University of Hong Kong, Hong Kong SAR, China*

[3]*College of Optical Sciences, University of Arizona, Tucson, Arizona 85721, USA*

[4]*Physics Department and Center for Optoelectronics and Photonics Paderborn (CeOPP), Universität Paderborn, Warburger Strasse 100, 33098 Paderborn, Germany*

[5]*Department of Physics, University of Arizona, Tucson, Arizona 85721, USA*

(Received 26 February 2013; published 20 May 2013)

We present a detailed theoretical study of transverse exciton-polariton patterns in semiconductor quantum well microcavities. These patterns are initiated by directional instabilities (driven mainly by polariton-polariton scattering) in the uniform pump-generated polariton field and are measured as optical patterns in a transverse plane in the far field. Based on a microscopic many-particle theory, we investigate the spatiotemporal dynamics of the formation, selection, and optical control of these patterns. An emphasis is placed on a previously proposed low-intensity, all-optical switching scheme designed to exploit these instability-driven patterns. Simulations and detailed analyses of simplified and more physically transparent models are used. Two aspects of the problem are studied in detail. First, we study the dependencies of the stability behaviors of various patterns, as well as transition time scales, on parameters relevant to the switching action. These parameters are the degree of built-in azimuthal anisotropy in the system and the switching (control) beam intensity. It is found that if the parameters are varied incrementally, the pattern system undergoes abrupt transitions at threshold parameter values, which are accompanied by multiple-stability and hysteresis behaviors. Moreover, during a real-time switching action, the transient dynamics of the system, in particular, the transition time scale, may depend significantly on the proximity of unstable patterns. The second aspect is a classification and detailed analysis of the polariton scattering processes contributing to the pattern dynamics, giving us an understanding of the selection and control of patterns as results of these processes' intricate interplay. The crucial role played by the (relative) phases of the polariton amplitudes in determining the gains and/or losses of polariton densities in various momentum modes is highlighted. As a result of this analysis, an interpretation of the actions of the various processes in terms of concepts commonly used in classical pattern-forming systems is given.

DOI: 10.1103/PhysRevB.87.205307 PACS number(s): 71.35.−y, 71.36.+c, 78.67.De, 42.70.Nq

I. INTRODUCTION

Laser beams propagating through a nonlinear medium can under certain conditions undergo directional instabilities. These instabilities are driven by phase-conjugate wave-mixing processes,[1–8] leading to spontaneous generation and build-up of intensity in modes with propagation directions other than those of the input beams. The system's transverse translational symmetry is thus spontaneously broken, resulting in periodic or quasiperiodic modulational patterns, e.g., stripes and hexagons, in the intensity profile. These spontaneously formed optical patterns have been observed in experiments with lasers,[9,10] and such passive optical systems as atomic gases,[11–14] liquid crystal light valves,[15] photorefractive crystals,[16] and, most recently, semiconductor quantum well microcavities.[17] (For general reviews, see, e.g., Refs. 18–20.) In a broader context, these developments are instances of spontaneous pattern formation found in a wide range of nonequilibrium physical systems such as classical fluids and chemical reaction systems.[21,22]

The occurrence of directional instability patterns in optics has also indicated the potential of using them for low-intensity all-optical switching. It was demonstrated in Ref. 14 that the orientation of transverse patterns in a rubidium vapor can be all-optically and reversibly switched by the application of a weak control beam. Subsequently, it was proposed that a similar switching scheme can also be implemented in a semiconductor quantum well microcavity.[8] Another analysis also shows the possibility to optically control transverse patterns in planar semiconductor structures.[7] A review of these activities was given in Ref. 23. The switching scheme devised in Ref. 8 has recently been experimentally demonstrated in a quantum well double-cavity system.[17] In this context, it is worthwhile to note the different physical origins of pattern formation in these systems. In an optically excited atomic vapor,[14] nonlinearities stem from partial saturation of the atomic resonances, and three-dimensional phase-matching conditions have to be satisfied with counterpropagating pump beams for efficient off-axis four-wave mixing of light to take place. In contrast, in a planar quantum well based microcavity, nonlinearities arise from the parametric scattering of exciton-polaritons[24–26] (polariton four-wave mixing), which is predominantly driven by the Coulomb interaction between the polaritons' excitonic constituents,[27–30] with additional smaller contributions from phase-space filling. Two-dimensional phase matching, in the cavity's plane, has to be fulfilled to render the scattering processes efficient.

While setting the conceptual foundation of the directional switching action in semiconductor microcavities in Ref. 8

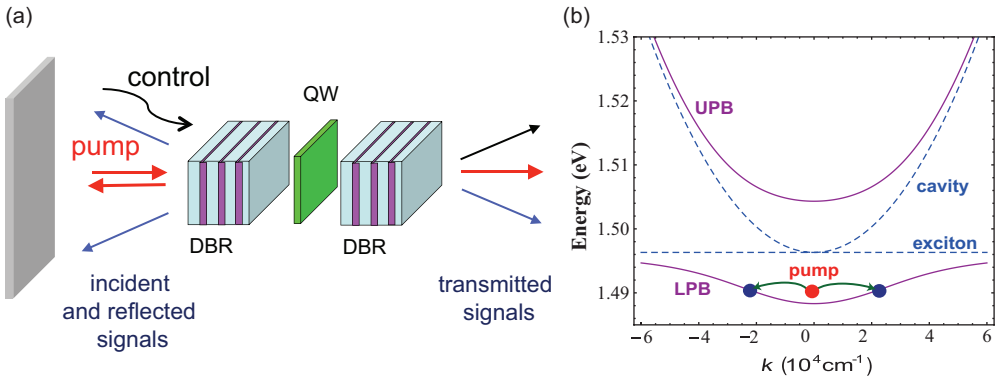

FIG. 1. (Color online) (a) Sketch of the semiconductor quantum well microcavity. Two distributed Bragg reflectors (DBR) form a photonic cavity with an embedded semiconductor quantum well (QW). The pump is in normal incidence to the quantum well plane. When transverse instabilities are present, off-axis patterns can be observed in the far field. The orientations of these patterns can be rotated by applying a weak control beam. (b) Cavity polariton energy vs in-plane momentum. The uncoupled exciton and cavity photon modes are shown as dotted and dashed lines, respectively. The solid lines represent the upper (UPB) and the lower (LPB) polariton branches. The displayed dispersion relations do not include the effects of (nonlinear) exciton interactions. The pump frequency and scattering of two pump-induced polaritons to off-axis modes are also indicated.

and implementing the switching in Ref. 17 were important steps forward, further work is required to fully understand the underlying complicated dynamics. In this paper, we study this problem theoretically as an instance of competitions among various transverse patterns formed by the nonlinear interactions of exciton polaritons. The switching action of the control beam is viewed as destabilizing the initial pattern while stabilizing another. Two aspects of this investigation are reported in this paper. First, we study the dependencies of the stability behaviors of various patterns, as well as transition time scales, on parameters relevant to the switching action. These parameters are the degree of built-in azimuthal anisotropy in the system and the control beam intensity. Second, we analyze in detail the actions of physical processes contributing to the dynamics and form an understanding of the selection and control of patterns as results of these processes' intricate interplay.

The nonlinear optical and many-boson aspects of polaritons in semiconductor microcavities are an active area of current research.[31] Besides modulational intensity patterns, more complicated spatial instability structures such as solitons[32] and vortices[33] are also being investigated in these systems. Optical parametric oscillation in various pump/signal configurations have been demonstrated in quantum well microcavities.[34–36] This process shares a common underlying mechanism—parametric polariton scattering—with the directional instabilities studied here.

The quantum well microcavity configuration used in this paper is sketched in Fig. 1(a). A photonic cavity is formed by a pair of distributed Bragg reflectors (DBRs), and a semiconductor quantum well (QW) is placed inside the cavity. One cavity photon mode is tuned to coincide with the lowest 1s heavy-hole excitonic resonance, leading to strong coupling between the two and the formation of an upper (UPB) and a lower (LPB) polariton branches. The dispersion relations (energy versus in-plane momentum) of these linear optical excitations for the parameters used in this paper are plotted in Fig. 1(b). A pump beam comes in at normal incidence to the cavity's plane and is spectrally tuned above the bottom of the lower polariton branch but well below the bare exciton resonance. It excites (virtual) polaritons with zero in-plane momenta, pairs of which can scatter near resonantly into modes with finite, opposite transverse (in-plane) momenta on the LPB, as indicated in Fig. 1(b). The scattered polaritons have a certain probability to emerge from the microcavity as photons. Under favorable conditions, when the pump intensity is above a threshold, the emerging photons in the off-axis directions become intense and coherent beams, characteristic of parametric, directional instabilities of the pump beam. The instability reduces the system's symmetry from transverse translational to azimuthal. This azimuthal symmetry may be further broken by the nonlinear interactions among the off-axis polariton field amplitudes, thereby favoring patterns with density in a finite number of clusters of **k** modes (i.e., modes in transverse momentum space), e.g., a hexagon or its subsets. Schematically illustrated in Fig. 2, the low-intensity switching scheme proposed in Ref. 8 involves transitions between two

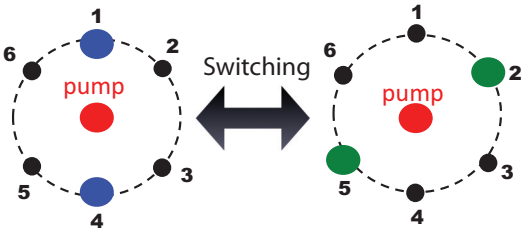

FIG. 2. (Color online) Schematic representation of the switching process. The sites labeled 1 to 6 represent the projected positions on a transverse plane in the far field of six off-axis momentum modes, forming a hexagon. On the left, an optical pattern is shown with the mode pair 1 and 4 being spontaneously generated by phase-conjugate instabilities and favored by a built-in anisotropy of the system. When a control beam is directed at mode 2, the pattern is rotated to directions 2 and 5. When the control is then turned off, the pattern reverts to its original orientation.

two-spot patterns residing on the same hexagon. (Note the role of the built-in azimuthal anisotropy in the preparation of the initial pattern.) Instead of coherent polariton scattering, the instabilities may equivalently be interpreted as arising from phase-conjugate four-wave mixing of the coherent polariton field.

The conditions for the formation of hexagons and two-spot patterns are quite well understood in other disciplines of physics.[21] However, the additional degrees of complexity, anisotropy and external real-time control, make pattern formation in our system, and in the system in Ref. 14, a much more involved issue than found in commonly studied systems. Moreover, unlike macroscopic pattern-forming systems, where the field is real valued, our polariton field is quantum mechanical and therefore complex valued, and the mutual activating and inhibiting actions of the mode densities on each other are entwined with their relative phases. This makes building physical intuition about these actions and hence how patterns are selected a nontrivial exercise.

Our theoretical approach is based on a microscopic theory of excitonic optical response of the semiconductor quantum well[27,28] coupled to a classical treatment of the light field. Only pairwise interactions among excitons, evaluated in the Hartree-Fock (HF) approximation, and Pauli blocking modifications of the light-exciton coupling are included in the nonlinear exciton dynamics. The theory is discussed in more detail in Sec. II below. To facilitate conceptual understanding, we treat only the simple case of a circularly polarized polariton field in a single quantum well cavity (see Fig. 1). Owing to the spin dependence of the exciton-exciton interaction,[28] the parametric scattering for linearly polarized polaritons is different from that in the circularly polarized case.[37] There are indications[17,35,37] that transverse instabilities are more favored in the linearly polarized case. Moreover, using a double cavity also makes pattern formation easier.[17] We believe the conclusions drawn in this paper about physical mechanisms also apply to these more complicated cases.

We solve the equations of our theory in various model state spaces. At the most complete level, we solve the real($\mathbf{r}$)-space version of our equations directly on a grid. While such simulations are realistic, they are computationally demanding and it is not easy to disentangle the roles played by various dynamical processes in generating the results. For this latter purpose, we also evaluate the theory within reduced model state spaces consisting of small numbers of $\mathbf{k}$ modes, the relative simplicity of which makes them much more amenable to analysis. In our parameter-dependency study and our analysis of the contributing dynamical processes, we make heavy use of a single-hexagon model that has a state space consisting of one pump mode ($\mathbf{k} = \mathbf{0}$) and six off-axis $\mathbf{k}$ modes arranged in a regular hexagon. Larger models are also used to analyze competitions among hexagons and more extended patterns.

This paragraph and the next summarize our findings. For typical GaAs parameters, even if the system has complete azimuthal isotropy, a ring pattern in momentum space is destabilized in favor of a single hexagon with arbitrary orientation. A small anisotropy is sufficient to destabilize the hexagon in favor of a two-spot pattern. As one increases the anisotropy continuously from zero, the transition from hexagon to two-spot is abrupt, and below this transition, a range of anisotropy values exist where both patterns are stable. In the switching scheme, a two-spot pattern stabilized by anisotropy is set up as the initial signal, and the control beam is directed at another mode pair (see Fig. 2). For our chosen material (GaAs) and pump beam parameters, the pattern can be switched by a control beam of intensity 1/6500 times the intensity of the two-spot signal. In a detailed parameter variation study, when the control intensity is increased from zero, the stable state transits from the two-spot pattern favored by the anisotropy, through an asymmetric hexagon (i.e., a hexagon with asymmetric distribution of intensity), to the two-spot pattern favored by the control. The transitions are again abrupt, with a bistable region at each transition. The switching time scale is normally of the order of 1 ns but diverges as the control intensity approaches from above the higher critical value for transition.

The analysis of the mechanisms underlying these phenomena has yielded the following picture. The dynamics of the polariton amplitude in a particular (off-axis $\mathbf{k}$) mode is driven by pairwise scatterings for which the mode in question is one of the outgoing modes. We classify the processes as linear, quadratic, or cubic according to how many of the other three modes involved in the scattering are off-axis (see Fig. 14). The linear gain processes provide the basic instability mechanism to the pump-excited uniform polariton field. For a pump intensity slightly above threshold, the set of $\mathbf{k}$ modes experiencing linear instability growth form a ring of finite thickness around the origin in (in-plane) momentum space. As the polariton amplitudes grow in these modes, the quadratic and cubic scattering processes, which represent interactions among the off-axis modes, come into play. They drive the competitions among phase-conjugate mode pairs [pairs with equal but opposite momenta ($\mathbf{k}$ and $-\mathbf{k}$)], which in turn determines whether a particular pattern (ring, hexagon, two-spot, etc.) is stable. Because of momentum conservation, the quadratic scatterings take place only among off-axis modes that are on a regular hexagon (see Fig. 14 below), whereas the cubic processes are not subjected to this restriction. Therefore competitions among modes residing on different hexagons are driven only by the cubic processes. It is important to note that the scatterings occur among coherent amplitudes: the relative phases of the involved polariton amplitudes play a crucial role in determining whether a particular process contributes to a gain or a loss in density for the mode in question. Because of the complex feedback between the dynamics of the phase and the magnitude of the polariton field, it is difficult to cleanly disentangle the gain/loss effects of the different processes. Even so, from the simulation results one can still characterize their effects using concepts common in classical pattern forming systems as follows. For the typical GaAs parameters used here, the stability of the hexagonal pattern over two-spot patterns (in the isotropic case) indicates that the net effect of the quadratic processes is "cross-activating," i.e., the presence of density in one conjugate mode pair favors the increase of density in other mode pairs. The main effect of the cubic processes is to bring about saturation of the off-axis polariton density. One can subdivide them into "self-saturating" (the density in a conjugate mode pair inhibiting its own growth) and "cross-saturating" (the density in one mode pair inhibiting the

growth of density in other pairs) processes. The spontaneous breaking of the azimuthal symmetry of the system, favoring the radially localized hexagons over a ring pattern, indicates that the cross-saturating processes are stronger than the self-saturating ones.

The above findings are based mostly on analyses of models in which the pump intensity is infinitely localized in momentum space (in the mode $\mathbf{k} = \mathbf{0}$), or equivalently, uniformly distributed over the 2D real space of the cavity's plane, and the state space is truncated. Further investigations into the effects of a finite pump laser spot size and inclusion of more modes in the state space will be carried out within the full 2D real-space simulation model.

The paper is organized as follows. We first describe and discuss our theoretical approach in Sec. II. In Sec. III, we show a set of results from a 2D **r**-space simulation and discuss two reduced models in truncated sets of **k** modes. In Sec. IV, we introduce and validate the single-hexagon model through comparison with the previous models. In Sec. V, we present the effects of variations of anisotropy and control beam intensity on pattern selection and switching behavior in the single-hexagon model. In Sec. VI, we classify the scattering/four-wave mixing processes among the polariton modes, and the complex interplay of these processes are analyzed in Sec. VII. An analysis of the competitions among modes belonging to different hexagons is carried out in Sec. VIII. Section IX contains some concluding comments.

II. THEORY OF NONLINEAR OPTICAL RESPONSE OF A QUANTUM WELL MICROCAVITY

This section outlines the microscopic theory of the third-order nonlinear response of a quantum well microcavity, from which our working equations are derived. The theory can conceptually be divided into two parts: the nonlinear response of the quantum well to the presence of cavity photons and the coupling between the relevant cavity photon modes and the light field outside of the cavity. Since we work in the regime of strong linear coupling between the QW exciton and a cavity photon mode, it is beneficial to consider the polaritons as elementary excitations of the QW microcavity and the cavity's nonlinear response as being due to the interactions among the polaritons. For the theory of nonlinear QW optical response, a more detailed account can be found in, e.g., Refs. 27,28,38, and 39. An account of our present theory was given in Ref. 23.

In Ref. 23, our treatment of the passage of light into and out of the cavity, when a given polaritonic excitation is present inside the cavity, was only very briefly explained. We start this section with a fuller account of this part of our theory. Numerically, the most accurate way to propagate light waves across the microcavity is, of course, to solve the Maxwell equations throughout the DBR + QW structure using, e.g., a transfer matrix method[27,40,41] or a finite-difference time-domain method.[42] However, since we are concerned with obtaining an overall picture of parametric dependencies rather than simulating a specific experimental setup, we have chosen to use a simple model that approximates the wave propagation effects as a coupling between the radiation field outside of the cavity and the chosen cavity mode. We will call the former the "macroscopic field." In this model, the whole microcavity is treated as a zero-thickness structure, which confines both the cavity photon field and the exciton field in the longitudinal direction and lets them extend across the entire transverse plane. The effect of the cavity photon field on the macroscopic light field is represented as a "polarization density" in the wave equation governing the latter. Explicitly, we write the electric displacement of the macroscopic field (which includes the incident, reflected, and transmitted waves) as

$$\mathcal{D}(\mathbf{r},t) = \epsilon_0 n_s^2 \mathcal{E}(\mathbf{r},t) - \hbar t_c \mathbf{E}_{\mathrm{cav}}(x,y,t)\delta(z), \tag{1}$$

where $\mathcal{E}(\mathbf{r},t)$ is the macroscopic electric field, ϵ_0 is the vacuum permittivity, n_s is the refractive index of the substrate outside of the cavity, $\mathbf{E}_{\mathrm{cav}}(x,y,t)$ is the cavity photon field, and t_c is a coupling strength. For later convenience, the dimension of $\hbar t_c$ is chosen to be that of electric charge. In Eq. (1), we have set up a coordinate system in which the z axis is along the longitudinal direction and the cavity is positioned at $z = 0$.

The incident waves (pump and control) come in from the left and are all "+"-circularly polarized. The exciton spin states in the QW are quantized along the z axis so that an obliquely incident (+)-polarized beam may also generate excitons with the spin -1 which, after interacting with other excitons, may generate a (−)-polarized component in the outgoing waves. However, the polar angles of the off-axis beams are usually quite small, and we, for simplicity, ignore this complication and take all outgoing fields to be (+)-polarized. The algebraic development within the model is detailed in Appendix, with the following results. Under the assumption that each of the waves involved is a slowly varying envelope modulating a plane wave with a common carrier frequency ω_p, the electric field in the half-space $z < 0$ can be written in the form

$$\mathcal{E}(\mathbf{r},t) = \sum_{\mathbf{k}} e^{i(k_x x + k_y y)} \hat{\mathbf{e}}_+ \{E_{\mathbf{k},\mathrm{inc}}[t + k_z(k,\omega_p)z/\omega_p] - E_{\mathbf{k},\mathrm{refl}}[t - k_z(k,\omega_p)z/\omega_p]\},\ z < 0, \tag{2}$$

where $\mathbf{k} = (k_x, k_y)$, $k = |\mathbf{k}|$, and $k_z(k,\omega_p) = +\sqrt{\omega_p^2 n_s^2/c^2 - k^2}$, c is the light speed in vacuum, and $\hat{\mathbf{e}}_+$ is the unit helicity vector for the (+)-polarized field. For each transverse momentum $\mathbf{k}$, $E_{\mathbf{k},\mathrm{inc}}$ is the incident field and $E_{\mathbf{k},\mathrm{refl}}$ is the reflected field. In the $z > 0$ half-plane, the field can be written as

$$\mathcal{E}(\mathbf{r},t) = \sum_{\mathbf{k}} e^{i(k_x x + k_y y)} \hat{\mathbf{e}}_+ E_{\mathbf{k},\mathrm{trans}}[t - k_z(k,\omega_p)z/\omega_p],\ z > 0, \tag{3}$$

where $E_{\mathbf{k},\mathrm{trans}}$ is the transmitted field. The cavity field, which by our argument above is also (+)-polarized, is also decomposed into its spatial Fourier modes:

$$\mathbf{E}_{\mathrm{cav}}(x,y,t) = \sum_{\mathbf{k}} e^{i(k_x x + k_y y)} \hat{\mathbf{e}}_+ E_{\mathbf{k}}(t). \tag{4}$$

We stress that $E_{\mathbf{k}}(t)$ here denotes a momentum-space component of the cavity field and is not to be confused with the macroscopic field $\mathcal{E}(\mathbf{r},t)$. The $\mathbf{k}$ sums in Eqs. (2)–(4) range in principle over the whole (transverse) momentum space, but they are restricted to a finite set of $\mathbf{k}$ modes in the reduced-mode model calculations discussed in this paper. For each $\mathbf{k}$ mode, the transmitted ($E_{\mathbf{k},\mathrm{trans}}$) and reflected ($E_{\mathbf{k},\mathrm{refl}}$) light fields are

solved in terms of the incident ($E_{\mathbf{k},\mathrm{inc}}$) and the cavity ($E_{\mathbf{k}}$) fields in the Appendix. The result is

$$E_{\mathbf{k},\mathrm{trans}} = E_{\mathbf{k},\mathrm{inc}} - E_{\mathbf{k},\mathrm{refl}}, \tag{5}$$

$$E_{\mathbf{k},\mathrm{refl}} = -\frac{\hbar t_c}{2n_s c\epsilon_0}\frac{dE_{\mathbf{k}}}{dt}. \tag{6}$$

We next postulate the equation of motion of the cavity field under the actions of the macroscopic light and the exciton fields. In writing down the equation, we make the reasonable assumption that each transverse $\mathbf{k}$ mode of the cavity field, $E_{\mathbf{k}}$, is a simple oscillator driven linearly by the other two fields. The proportionality coefficients in the coupling terms are chosen in such a way that $|E_{\mathbf{k}}|^2$ can be interpreted as mode photon density (see Appendix). The equation is

$$i\hbar\frac{dE_{\mathbf{k}}}{dt} = \hbar\omega^c_{\mathbf{k}}E_{\mathbf{k}} - \Omega_{\mathbf{k}}p_{\mathbf{k}} + \hbar t_c E^{\mathrm{eff}}_{\mathbf{k},\mathrm{inc}}, \tag{7}$$

where $\omega^c_{\mathbf{k}}$ is the uncoupled mode dispersion relation for a cylindrically symmetric cavity: $\omega^c_{\mathbf{k}} = \sqrt{\omega^{c2}_{\mathbf{0}} + c^2k^2/n_b^2}$, $\omega^c_{\mathbf{0}}$ being the cavity mode energy at $\mathbf{k} = \mathbf{0}$, and n_b being an effective refractive index of the cavity's medium, which characterizes the transverse propagation speed of the cavity mode. $p_{\mathbf{k}}$ denotes the exciton field, which will be identified below with the $1s$ heavy-hole exciton contribution to the interband polarization in the QW, so that $|p_{\mathbf{k}}|^2$ is the exciton density (number of excitons per unit area) in the $\mathbf{k}$ mode. (Strictly speaking, $|p_{\mathbf{k}}|^2$ and $|E_{\mathbf{k}}|^2$ only represent the coherent parts of their respective densities, but since the incoherent densities are expected to be small and are ignored in this paper, we will drop the qualifier "coherent.") The exciton-photon coupling strength $\Omega_{\mathbf{k}}$ is an input parameter in Eq. (7), but will be given a microscopic meaning in terms of electron-hole dynamics below. $E^{\mathrm{eff}}_{\mathbf{k},\mathrm{inc}}$ is the (limiting value of the) macroscopic electric field at the cavity's position. Within our model, we have

$$E^{\mathrm{eff}}_{\mathbf{k},\mathrm{inc}}(t) = E_{\mathbf{k},\mathrm{trans}}(t). \tag{8}$$

The coupling coefficient t_c was introduced in Eq. (1) above. If we set the incident field $E_{\mathbf{k},\mathrm{inc}}$ and the exciton field $p_{\mathbf{k}}$ to zero, Eqs. (5)–(8) would reduce to a homogeneous equation for $E_{\mathbf{k}}$ from which we can extract a radiative decay rate (in energy units) $\Gamma = \omega_p\hbar^2t_c^2/(2\epsilon_0 cn_s)$ for the cavity. We reiterate that Eq. (7) is written down as a *postulate* based on physically reasonable assumptions. This treatment is sufficient for our purposes here. Alternatively, it could be derived as a classical approximation in a theory that starts with the cavity photon field being quantized.

We next briefly describe the microscopic theory of the excitonic optical response of quantum wells that gives the equation of motion of $p_{\mathbf{k}}$.[27,28,38,39] It starts with a many-particle Hamiltonian operating on the Fock space of electrons and holes. Referring to Fig. 1 again, for the quantum well, we consider a GaAs-type semiconductor band structure around the fundamental band gap with an exciton size of about 10^{-6} cm. For the present study, the single-particle basis includes only one parabolic conduction and one parabolic valence bands, i.e., the heavy-hole band. The Hamiltonian contains the charge carriers' kinetic energy, pairwise Coulomb interactions among them, and a coupling to the cavity photon field that either creates or annihilates an electron-hole pair in the rotating wave approximation. Thus the only material parameters in the theory are the electron mass, the hole mass, the background dielectric constant, and the interband dipole coupling. With this Hamiltonian, equations of motion of observables (certain expectation values of products of charge carrier creation/annihilation operators) are derived. The dynamical variable relevant to us, the exciton field $p_{\mathbf{k}}(t)$, is defined in this microscopic theory as the interband polarization restricted to the heavy-hole $1s$ exciton subspace:[28]

$$p_{\mathbf{k}}(t) = \frac{1}{\mathcal{L}^2}\sum_{\mathbf{k}'}\tilde{\phi}(\mathbf{k}' + \beta\mathbf{k})\langle a_{h,-\mathbf{k}'}(t)a_{e,\mathbf{k}'+\mathbf{k}}(t)\rangle, \tag{9}$$

where $a_{e,\mathbf{q}}(t)$ is the Heisenberg-picture annihilation operator of a conduction band electron with momentum $\mathbf{q}$ at time t and $a_{h,\mathbf{q}}(t)$ is the corresponding operator for a hole state, and $\langle\cdots\rangle$ represents the expectation value in the initial state of the electron-hole system. $\beta = m_h/(m_e + m_h)$ is the ratio of the hole mass to the total exciton mass, $\mathcal{L}^2$ is the area of the normalization box, and $\tilde{\phi}(\mathbf{q}) = \sqrt{2\pi}a_0/[1 + (a_0q/2)^2]^{3/2}$ is the two-dimensional internal $1s$ exciton wave function in the space of relative electron-hole momentum, with $a_0 = \hbar^2\epsilon_b/(e^2m_r)$, ϵ_b and m_r being the (3D) exciton Bohr radius, the background dielectric constant, and the reduced mass of the electron-hole pair respectively. The restriction to the $1s$ state is valid because we limit the pump intensity so that the maximum generated polariton density is of the order of 10^{10} cm^{-2}. At this density and the chosen pump frequency, which is tuned to a frequency within the lower polariton branch [see Fig. 1(b)], the excitations in the quantum well are expected to stay predominantly in the $1s$ heavy-hole exciton state. For a more detailed analysis on the validity of the $1s$ approximation, see Ref. 28. Since we restrict our considerations to (+)-polarized excitons, the electron and the hole in Eq. (9) have spins $-1/2$ and $3/2$, respectively.

Starting from the electron-hole vacuum as the initial state, the equation of motion for the $p_{\mathbf{k}}(t)$ is derived up to third order in the light field amplitude[38,39,43] on the Hartree-Fock-level. In the derivation, the single-pair electron-hole basis is restricted to the $1s$ state as mentioned. In this limit, the equation for a system of co-circularly-polarized excitons in the coherent third-order regime is[8,27,28]

$$i\hbar\frac{dp_{\mathbf{k}}}{dt} = \left(\varepsilon^x_{\mathbf{k}} - i\gamma_x\right)p_{\mathbf{k}} - \Omega_{\mathbf{k}}E_{\mathbf{k}} + \frac{1}{\mathcal{L}^2}\sum_{\mathbf{q}\mathbf{k}'\mathbf{k}''}(2\tilde{A}\Omega_{\mathbf{k}''}p^*_{\mathbf{q}}p_{\mathbf{k}'}E_{\mathbf{k}''} + V_{\mathrm{HF}}p^*_{\mathbf{q}}p_{\mathbf{k}'}p_{\mathbf{k}''})\delta_{\mathbf{q},\mathbf{k}'+\mathbf{k}''-\mathbf{k}}. \tag{10}$$

Here, $\varepsilon^x_{\mathbf{k}}$ is the free exciton energy and γ_x is a phenomenological dephasing rate, which represents all nonradiative losses, including the transfer of coherent excitons to the incoherent population. The photon-exciton coupling $\Omega_{\mathbf{k}}$, which is an input parameter in the cavity photon equation, Eq. (7), is given in the present microscopic theory by (in SI units)

$$\Omega_{\mathbf{k}} = e\langle r\rangle_{eh}\phi^*(\mathbf{0})f_\gamma(z_{\mathrm{QW}})\sqrt{\hbar\omega^c_{\mathbf{k}}/\epsilon_0\epsilon_b}, \tag{11}$$

where $\langle r\rangle_{eh}$ is the interband dipole matrix element, $\phi^*(\mathbf{0}) = 2\sqrt{2}/(a_0\sqrt{\pi})$ is the two-dimensional real space $1s$ exciton wave function [Fourier transform of $\tilde{\phi}(\mathbf{q})$] at zero electron-hole separation, $f_\gamma(z)$ is the resonant cavity photon wave function

along the coordinate axis (z axis) normal to the cavity's plane, normalized to unity: $\int_{-\infty}^{\infty} dz|f_\gamma(z)|^2 = 1$ and $z_{\rm QW}$ is the position of the quantum well on the z axis.

Of the two third-order terms, the term with the pp^*E structure stems from Pauli blocking, or phase-space filling (PSF), among the fermionic components of the exciton that are created by photon absorption and those of excitons already in the system. The strength is given by $\tilde{A} = 2\pi a_0^2/7$. The other term is due to mean-field, or Hartree-Fock (HF), Coulomb interaction among the excitons, with strength $V_{\rm HF} = 2\pi E_b a_0^2(1 - 315\pi^2/4096) \approx 1.52 E_b a_0^2$, where E_b is the (2D) exciton Rydberg energy. Both $\tilde{A}$ and $V_{\rm HF}$ actually depend on the momenta of the involved excitons and photons, but since the dependencies are rather weak and the relevant momenta are not excessively large, we approximate them by their values at zero momentum. Each exciton interaction or PSF term can be visualized as either a four-wave mixing process with wave-vector and frequency matching or a polariton-polariton scattering process with momentum and energy conservation. The full set of third-order terms also includes a time-retarded Coulomb correlation between two excitons, which is neglected here. Because of its time-nonlocal structure, including the Coulomb correlation term in Eq. (10) would increase the complexity in solving the equation substantially. It was previously shown[27,28] that it is much less important than the PSF and HF terms when the two interacting excitons are co-circularly polarized and have energies far below the exciton resonance. So dropping the retarded-Coulomb term in our case is expected to be a good approximation. A detailed study of its effects on polariton pattern formation will be a subject for future work.

Moreover, the dynamical effects of the dephased excitons are not considered. A more comprehensive theory would include a description of the transfer by dephasing and the subsequent interactions between the coherent and incoherent populations. Equations of motion serving this purpose could be derived within the microscopic frameworks that produce Eq. (10). While recent experiments indicate that the incoherent exciton population remain small[36] in the density and frequency regions that we consider, its cumulative effects should be studied more carefully. Similar considerations apply to three-exciton and larger-cluster correlations, which would be accounted for in an extended theory beyond the $\chi^{(3)}$ regime.

To recapitulate, Eqs. (5)–(8) and (10) are the working equations in the present paper. With the incident macroscopic light field $E_{\mathbf{k},\rm inc}(t)$ as input, the response of the quantum well microcavity, $E_{\mathbf{k}}(t)$ and $p_{\mathbf{k}}(t)$, as well as the resulting output light fields, $E_{\mathbf{k},\rm trans}(t)$ and $E_{\mathbf{k},\rm refl}(t)$, are calculated by solving this set of equations simultaneously.

III. SIMULATIONS AND REDUCED MODELS

In this section, we show some representative numerical results on transverse pattern competition and control in a quantum well microcavity by solving, at various levels of approximation, Eqs. (5)–(8) and (10) laid down in the previous section. To set the stage for our discussion, we first summarize in Sec. III A the linear instabilities of the pump-induced uniform steady state against finite-$|\mathbf{k}|$ fluctuations. We will then present in Sec. III B a set of representative results of our full two-dimensional simulations, showing the formation of a hexagonal pattern. We will next introduce, in Sec. III C, two reduced models—the "multi-$|\mathbf{k}|$" and the "ring" models—in which the equations of motion are solved over selected sets of $\mathbf{k}$ modes. These two models essentially reproduce the representative results of the full 2D simulations. We will extend our investigations using these models, presenting, in particular, a switching process between two patterns controlled by a weak applied beam. Based on these investigations, we will argue at the end of this section that the analysis of an even simpler model, the state space of which consists of the $\mathbf{k} = \mathbf{0}$ mode and a hexagonal set of six off-axis modes, could be expected to provide the critical insights to understand the patterns' behaviors in the more comprehensive models. This "single-hexagon" model will be analyzed in detail in the following sections.

For the calculations, material parameters appropriate for GaAs are used: $E_b \approx 13$ meV, $a_0 \approx 170$ Å, $\varepsilon_{\mathbf{0}}^x = 1.497$ eV, $\gamma_x = 0.4$ meV, $\Omega_k \equiv \Omega = 8$ meV, $n_s = n_b = 3.6$, and $\epsilon_b = n_b^2$. With the given values of E_b and a_0, $V_{\rm HF} \approx 0.57 \times 10^{-10}$ meV cm^2, and $2\tilde{A}\Omega$ is about three times weaker. For the cavity mode, we choose $\hbar\omega_{\mathbf{0}}^c = \varepsilon_{\mathbf{0}}^x$, and t_c is chosen such that the radiative decay rate is $\Gamma \approx 1.5$ meV for $\hbar\omega_p$ around 1.5 eV. The incident pump is tuned to 5 meV below the bare exciton resonance, i.e., $\hbar\omega_p = 1.492$ eV, and its steady-state flux intensity, which we denote by $I_{\rm pump}$, is about 91.0 kW cm^{-2}.

A. Linear instabilities of the uniform polariton state

The linearized Eqs. (7) and (10) at the lossless limit, i.e., with $V_{\rm HF}$, $\tilde{A}$, γ_x, and t_c set to zero, give the linear polariton spectrum and the polariton eigenvectors in the photon-exciton basis. With the other parameters set as above, the linear polariton spectrum is plotted in Fig. 1. Returning to the full nonlinear equations, one can easily verify that when the input field is incident normally on the cavity (pump only), there exist solution(s) that preserve the planar translational symmetry of the input beam ($p_{\mathbf{k}}$ and $E_{\mathbf{k}}$ vanish for all $\mathbf{k} \neq \mathbf{0}$). At steady state, $p_{\mathbf{0}}$ and $E_{\mathbf{0}}$ oscillate at the pump frequency ω_p. The exciton density $|p_{\mathbf{0}}|^2$ calculated for the above parameter values is plotted as a function of the incident field intensity $I_{\rm pump} = 2cn_s\epsilon_0|E_{\mathbf{0},\rm inc}|^2$ in Fig. 3. A linear stability analysis with off-axis ($\mathbf{k} \neq \mathbf{0}$) perturbations on the uniform solution is performed, and the range of instability against this class of perturbations is also shown in Fig. 3. The stability matrix is block diagonal in $\mathbf{k}$ space with the fields $p_{\mathbf{k}}$, $E_{\mathbf{k}}$, $p_{-\mathbf{k}}$, and $E_{-\mathbf{k}}$ for each $\mathbf{k}$ coupled together. For each value of $|p_{\mathbf{0}}|$ within the off-axis instability range, the uniform state is unstable against small random perturbations in a set of $\mathbf{k}$ modes, which form a ring of finite radial thickness in $\mathbf{k}$ space. The mean radius of this ring is approximately determined by phase matching that fulfills the resonance in the polariton scattering, as illustrated in Fig. 1(b). The dispersion relations in Fig. 1(b) are calculated without the exciton interactions in Eq. (10), which shift the exciton energy, and hence the (lower) polariton energy, upwards. As a result, the actual resonant $|\mathbf{k}|$ value is smaller than that shown in Fig. 1(b). The point $(|E_{\mathbf{0},\rm inc}|, |p_{\mathbf{0}}|)$ corresponding to the incident field strength used in our calculations is marked in Fig. 3. For this value, the instability-triggering $\mathbf{k}$ modes lie in the range 1.25×10^{-4} cm$^{-1} \leqslant |\mathbf{k}| \leqslant 1.40 \times 10^{-4}$ cm^{-1}.

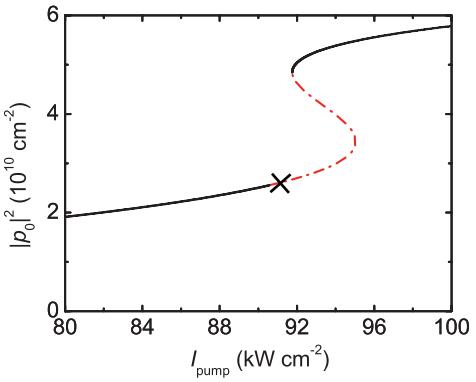

FIG. 3. (Color online) Steady-state pump-generated exciton density in the quantum well as a function of the pump beam intensity. For densities inside the red, dashed segment, the uniform polariton field is unstable against finite $|\mathbf{k}|$ perturbations. The cross marks the pump intensity used in the simulations here.

More detailed discussions of the linear stability analysis of the uniform state may be found in Refs. 37 and 44. In our calculations, starting from the uniform state under steady pump irradiation, the polariton field (the lower polariton branch) for each mode inside the "ring of instability" initially grows in time exponentially from random fluctuations. Subsequently, the interactions among these off-axis polariton modes, and the $\mathbf{k} = \mathbf{0}$ mode, govern the long-time competition dynamics among them.

B. 2D real-space simulations

The full 2D simulations are performed in real space by solving the Fourier transforms of Eqs. (7) and (10). We show a representative set of results here. A more comprehensive discussion of these simulations will be presented in a future publication. The configuration space is a square (spatial) grid with a step size of $\Delta x = \Delta y = 0.45\,\mu$m in a box of length 90 μm on one side. The initial state of the system is the polariton "vacuum," i.e., the ground state of the semiconductor microcavity. The pump beam is switched on at $t = 0$, its intensity becoming steady after 8 ns. Shown in Fig. 4(a), the steady-state pump profile is broad and flat so that its corresponding (transverse) momentum distribution is narrowly

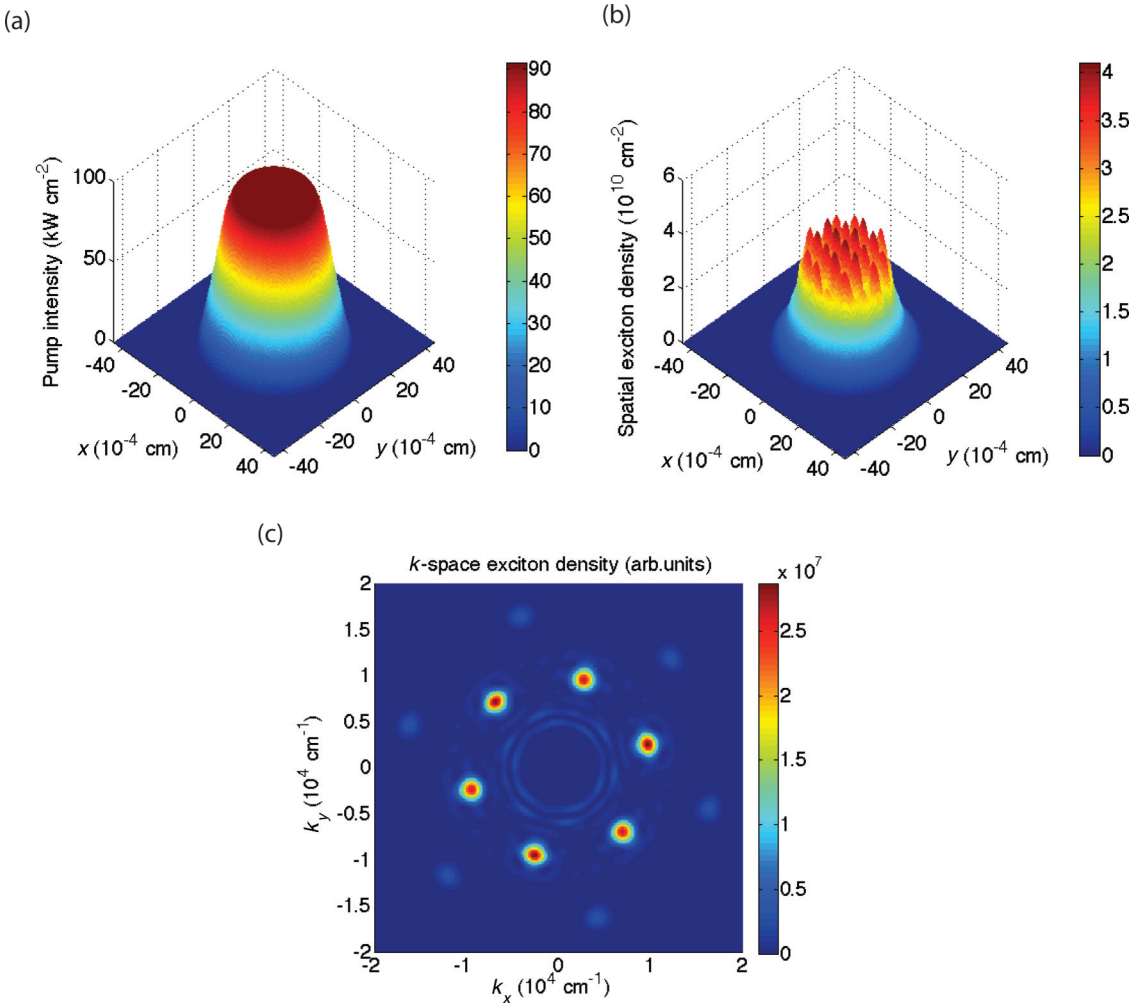

FIG. 4. (Color online) Two-dimensional real-space simulations of hexagonal pattern formation. (a) The pump profile in two-dimensional real space. (b) The exciton density profile in the QW with modulations stemming from transverse instabilities. (c) Hexagonal pattern in transverse momentum space formed by the exciton field in (b). The density in the center (in the pump mode) has been masked for clarity. See text for details of the simulations.

peaked at $\mathbf{k} = \mathbf{0}$. As time progresses, coherent polariton amplitudes in several off-axis $\mathbf{k}$ modes form "spontaneously," causing density patterning inside the cavity. The calculated real-space exciton density distribution inside the QW at $t =$ 18 ns is shown in Fig. 4(b). The corresponding momentum distribution is plotted in Fig. 4(c), which shows a dominant hexagonal pattern situated within the ring of linear instability. The azimuthal orientation of the hexagon is random.

C. Reduced models

The linear off-axis instability spontaneously breaks the (transverse) translational symmetry of the system's setup but preserves the latter's azimuthal symmetry. In the full 2D simulations, when the off-axis polariton fields are being built up, their mutual interactions also break the azimuthal symmetry, resulting in a stable hexagonal structure. As explained above, the simulation results indicate that the collection of modes taking part in the pattern dynamics are relatively localized in $\mathbf{k}$ space. We take advantage of this fact and use reduced models in the following to investigate the competitions among different patterns, their control, and the physical mechanisms underlying these competitions.

In the reduced models, we restrict our state space to a selected finite set of $\mathbf{k}$ modes. We introduce two such models in this section. (i) The multi-$|\mathbf{k}|$ model: for the state space in this model, we choose six directions corresponding to the vertices of a regular hexagon centered at $\mathbf{k} = \mathbf{0}$. The hexagon's orientation is arbitrary. N evenly spaced points along a radial segment in each direction are included in the state space, as illustrated in Fig. 5(a). Explicitly, we write the $\mathbf{k}$ points as

$$\mathbf{k}_{h,i} = (k_0 + h\delta k)\hat{\mathbf{e}}_i,\ h = 1,\ldots,N,\ i = 1,\ldots,6, \quad (12)$$

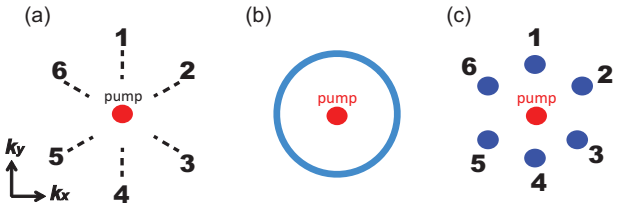

FIG. 5. (Color online) Sketches of the state spaces, made up of modes in transverse momentum space, of the three reduced models used in this paper. (a) Multi-$|\mathbf{k}|$ model: beside the origin, the modes lie on six radial segments (thick dashed lines) arranged hexagonally. (b) Ring model: the off-axis part of the state space is a ring of linearly unstable $\mathbf{k}$ modes. (c) Single-hexagon model: the state space is the origin plus a six-mode subset of the ring model state space that form a regular hexagon.

where $\hat{\mathbf{e}}_i, i = 1,\ldots,6$ are unit vectors in the vertex directions, and the minimum radius k_0 and the grid size δk are run-time parameters in the numerical calculations. (ii) The ring model: in this model, we choose the $|\mathbf{k}|$ modes to lie on a circle centered at the origin, regularly spaced in the angle coordinate, as illustrated in Fig. 5(b). We also organize the points into N hexagons, writing them as

$$\mathbf{k}_{h,i} = k_r\hat{\mathbf{e}}_{h,i},\ h = 1,\ldots,N,\ i = 1,\ldots,6, \quad (13)$$

where $\hat{\mathbf{e}}_{1,i}$ is a unit vector in an arbitrarily selected direction, $\hat{\mathbf{e}}_{h+1,i}$ is obtained by rotating $\hat{\mathbf{e}}_{h,i}$ counterclockwise through the angle $\frac{\pi}{3N}$, and the radius of the circle, k_r, is a run-time parameter.

By considering the momentum conservation constraint in the nonlinear terms in Eq. (10), one can see that, for both models, Eq. (10) reduces to equations of the following form (we have simplified the notation $p_{\mathbf{k}_{h,i}}$ to $p_{h,i}$ and $p_{\mathbf{0}}$ to p_0): the $\mathbf{k} = 0$ (on-axis) equation reads

$$i\hbar\dot{p}_0 = \left[\varepsilon_0^x - i\gamma_x + V_{\mathrm{HF}}\left(|p_0|^2 + 2\sum_{h,i}|p_{h,i}|^2\right) + 2\tilde{A}\Omega\sum_{h,i}p_{h,i}^*E_{h,i}\right]p_0 - \Omega\left[1 - 2\tilde{A}\left(|p_0|^2 + \sum_{h,i}|p_{h,i}|^2\right)\right]E_0$$
$$+ p_0^*\sum_{h,i}(2\tilde{A}\Omega p_{h,i}E_{h,i+3} + V_{\mathrm{HF}}p_{h,i}p_{h,i+3}) + 2\sum_{h,i}p_{h,i}^*[\tilde{A}\Omega(p_{h,i+1}E_{h,i-1} + p_{h,i-1}E_{h,i+1}) + V_{\mathrm{HF}}p_{h,i+1}p_{h,i-1}]. \quad (14)$$

The off-axis equations, for $h = 1,\ldots,N$ and $i = 1,\ldots,6$, read

$$i\hbar\dot{p}_{h,i} = \left[\varepsilon_{h,i}^x - i\gamma_x + 2V_{\mathrm{HF}}\left(|p_0|^2 - \frac{1}{2}|p_{h,i}|^2 + \sum_{h',i'}|p_{h',i'}|^2\right) + 2\tilde{A}\Omega\left(p_0^*E_0 + \sum_{h',i'}p_{h',i'}^*E_{h',i'}\right)\right]p_{h,i}$$
$$- \Omega\left[1 - 2\tilde{A}\left(|p_0|^2 - |p_{h,i}|^2 + \sum_{h',i'}|p_{h',i'}|^2\right)\right]E_{h,i} + 2p_{h,i+3}^*\left\{\tilde{A}\Omega\left[p_0E_0 + \sum_{h',i'}p_{h',i'}E_{h',i'+3}\right.\right.$$
$$\left.\left. - (p_{h,i}E_{h,i+3} + p_{h,i-3}E_{h,i})\right] + V_{\mathrm{HF}}\left[\frac{1}{2}p_0^2 + \sum_{h'}(p_{h',i+1}p_{h',i-2} + p_{h',i+2}p_{h',i-1}) + \sum_{h'\neq h}p_{h',i}p_{h',i-3}\right]\right\}$$
$$+ 2p_0^*[\tilde{A}\Omega(p_{h,i+1}E_{h,i-1} + p_{h,i-1}E_{h,i+1}) + V_{\mathrm{HF}}p_{h,i+1}p_{h,i-1}] + 2p_0[\tilde{A}\Omega(p_{h,i+2}^*E_{h,i+1} + p_{h,i-2}^*E_{h,i-1})$$
$$+ V_{\mathrm{HF}}(p_{h,i+2}^*p_{h,i+1} + p_{h,i-2}^*p_{h,i-1})] + 2\tilde{A}\Omega(p_{h,i+2}^*p_{h,i+1} + p_{h,i-2}^*p_{h,i-1})E_0. \quad (15)$$

When the off-axis direction number subscript i is outside the range 1–6, it represents the direction either $i - 6$ for i greater than 6 or direction $i + 6$ for i smaller than 1. For simplicity, we have neglected the $\mathbf{k}$ dependence of $\Omega_{\mathbf{k}}$ and replaced it by $\Omega = \Omega_{\mathbf{0}}$. The cavity field equations, Eqs. (5)–(8), remain the same for each $\mathbf{k}_{h,i}$, with analogous notations being used for the cavity and macroscopic fields: $E_{h,i}$, etc.

On the right-hand side of Eq. (14), the $\chi^{(3)}$ terms represent, in the order of their appearance, the HF shift in the exciton energy, photon scattering off an exciton density grating, Pauli blocking of the photon-exciton coupling, and various density transferring scattering processes. The terms in Eq. (15) can also be interpreted the same way. We will discuss the density transferring processes in more detail below.

1. *The multi-|k| model: results*

Within this model, we explore the competitions among patterns that exist in a hexagonal geometry and the radial distributions of these patterns in $\mathbf{k}$ space. The state space consists of $N = 256$ points in the direction of each of the six hexagonal vertices. We use a grid size of 22.5 cm^{-1} along each radial segment so that the state space is spread over the range from 1.10675×10^4 to 1.6805×10^4 cm^{-1} in each segment. In this state space, Eqs. (5)–(8), (14), and (15) are solved in the rotating frame of the incident field, i.e., with $e^{-i\omega_p t}$ factored out of all the fields in the equations. The time stepping is performed with the fourth-order Runge-Kutta method with a time step of 20 fs. This time step is sufficient for simulating the system dynamics, which has a typical time scale of the order of 1 ps, with good accuracy. Random fluctuating light sources (4.55×10^{-6} W cm^{-2}) are added in the off-axis modes as seeds for the initial instability growth.

Solving this model with the same material and beam parameters as in the full 2D simulations yields similar results, i.e., starting with the 2D uniform state, the system spontaneously generates off-axis coherent fields which subsequently stabilize as a hexagonal pattern. Along each radial segment, the off-axis field initially grows in modes over a range of $|\mathbf{k}|$ values. When the pattern is stabilizing, however, one mode in each hexagonal direction wins, the intensity in the other modes in the segment decaying to zero.

In the experiment using atomic vapors in Ref. 14, a stable two-spot pattern was obtained instead of a hexagon. It was theorized that an imperfect azimuthal symmetry, which is unavoidable in practice, might have favored the two-spot pattern. In the theoretical calculations on microcavities in Ref. 8, it was found that a small anisotropy introduced in one orientation is sufficient to favor the two-spot over the more symmetric distribution over all six hexagonal directions, and the subsequent controlled switching involves another two-spot pattern. For a recent detailed discussion of anisotropy in a real system, see Ref. 45.

We have carried out calculations for this slightly anisotropic situation. The anisotropy is imposed, as in Ref. 8, by lowering ω_k^c by 0.12 meV in directions 1 and 4 at every $|\mathbf{k}|$. The values of other parameters remain as set above. A set of numerical results that include reversible switching by a control beam are shown in Fig. 6. The top three panels show the light intensities reflected from the microcavity in the six off-axis directions,

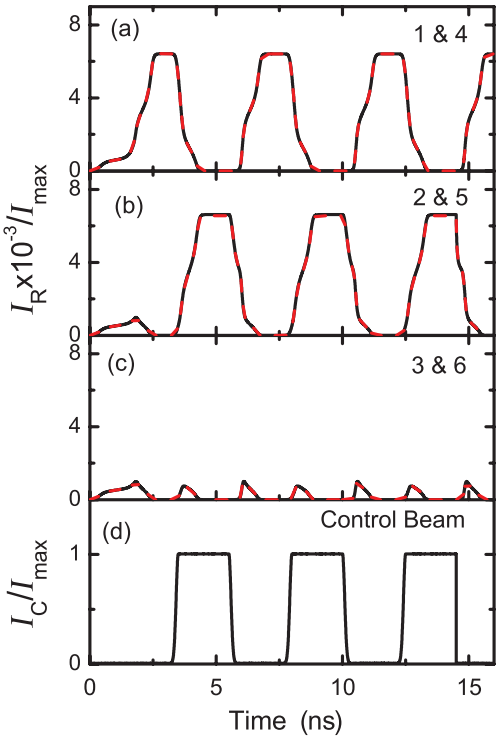

FIG. 6. (Color online) (a)–(c) Reflected signals (I_R), summed over radial $\mathbf{k}$ modes, vs time in the off-axis directions of the multi-$|\mathbf{k}|$ model. The directions of the signals in each panel are marked by numerical labels, which are defined in Fig. 1(a). Black solid lines represent the signals in directions 1–3 and the red dashed lines those in directions 4–6. $I_{max} = 3.3 \times 10^{-2}$ W $\text{cm}^{-2} = 3.6 \times 10^{-7} I_{pump}$ denotes the peak control intensity. (d) The control beam intensity (I_C) vs time.

and the bottom panel shows the control beam, as functions of time. In each direction, the intensity has been summed over all the modes on the radial segment in Fig. 5(a). The simulation starts at time $t = 0$ with all fields equal to zero except for some low-level fluctuations. The external pump field is turned on in the $\mathbf{k} = \mathbf{0}$ mode and reaches its steady state at about 30 ps with $|p_0|^2 = 2.6 \times 10^{10}$ cm^{-2}. The pump steady-state intensity is just above the instability threshold, leading to the build-up of field intensity in the off-axis modes. The build-up occurs in all six directions initially, but after a while, the asymmetry (anisotropy) introduced in the cavity mode's dispersion relation gives a decisive advantage to directions 1 and 4, where the field intensity continues to grow to a steady state at around $t \approx 2.7$ ns, while the intensities in the other four directions fall back to fluctuation level. A control beam of intensity $= 3.3 \times 10^{-2}$ W $\text{cm}^{-2} = 3.6 \times 10^{-7} I_{pump}$ is introduced in direction 2 (see below for the radial $|\mathbf{k}|$ value of the control) at $t = 3$ ns, and it switches the off-axis intensity to directions 2 and 5, reaching a steady-state level after 1.6 ns. In the switching process, the instability-generated field intensity is about 6500 times stronger than the control intensity. The control beam is then turned off at $t = 5.5$ ns, whereupon the signal reverts to directions 1 and 4, reaching steady state at $t = 7.0$ ns. This reversible switching process can be repeated indefinitely, as shown. We recall that the energy-scale parameters, i.e., $V_{HF}|p_0|^2$, γ_x etc, in the polariton

equations (7), (14), and (15) are of order of meV, giving a natural dynamical time scale of a picosecond. However, the (linear) gain and loss rates in the off-axis modes offset each other by roughly two orders of magnitude (the pump intensity level is set here slightly above threshold) so that the changes in polariton density happen on a longer-time scale between several tens of picosecond to nanosecond. Another point to note is, when the control is turned on or off, it affects not just the fields in directions 1,4 and 2,5. Every time the control changes, the field in the third direction pair 3 and 6 grows and then decays to zero. Concurrent to this movement, the intensities in 1,4 and 2,5 undergo a slower change, forming a shoulder on each of the time traces. These results are qualitatively similar to those in Ref. 8, but quantitatively dramatically different, in that the intensity ratio of the switched signal to the control beam in the present calculation is about two orders of magnitude larger than in Ref. 8. This improvement is attained by raising the radiative decay rate of the cavity from $\Gamma = 0.4$ meV in Ref. 8 to $\Gamma = 1.5$ meV here, other parameters being the same.

Figure 7 shows radial ($|\mathbf{k}|$) distributions of intensity in directions 1 and 2 as functions of time. At about $t = 0.2$ ns, instability-generated fields appear in a range of radial shells in all six directions. At $t \approx 1.7$ ns, the distribution is narrowed to a single $|\mathbf{k}|$ mode, which we label by h_0, in each direction. (Under certain conditions, instability occurs in one of the two adjacent $|\mathbf{k}|$.) The polariton frequency of this mode, including the effect of the pump-induced HF and PSF shifts, is approximately in resonance with the pump frequency. Afterwards, as shown in Fig. 6, the intensity in direction 1 and $h = h_0$ rises to a steady-state value while that in direction 2 falls to almost zero. The control beam is directed at the mode with momentum $\mathbf{k} = \mathbf{k}_{h_0,2}$. Figure 7 shows the reversible directional switching. As can be seen, there is no spreading of the intensity distribution over the radial modes during the switching to direction 2 or the subsequent return switching to direction 1.

The convergence of the off-axis signals in each direction to a single radial momentum mode is an important feature of the multi-$|\mathbf{k}|$ model simulation results. This implies that a further reduced model, in which only one mode is included in each hexagonal direction, would be adequate in analyzing the competitions among patterns in a hexagonal state space and the switching process. We call this simpler model the "single-hexagon model" and will use it in the following sections to carry out a parameter-variation study of the pattern competitions and analyze their underlying physical mechanisms. In the full 2D simulations, the convergence to one radial momentum mode is not as evident, which may be due to the fact that the pump beam is a finite-width distribution in $\mathbf{k}$ space in the 2D simulations instead of a single mode (at $\mathbf{k} = \mathbf{0}$) as in the present model. Results similar to those in Fig. 6 have been presented in Ref. 8, but were not analyzed in detail.

2. *The ring model: results*

In the ring model, we consider modes described by Eq. (13) with $k_r = 1.2935 \times 10^4$ cm^{-1}, which is the winning radial momentum extracted from the multi-$|\mathbf{k}|$ model (see Fig. 7). All parameters are the same as in the full 2D simulations; in particular, no spatial anisotropy is given to any mode here. Low-level random seed fluctuations in the field are put into the off-axis modes. Instability-induced fields initially grow in all modes around the ring, but eventually, as in the full 2D simulations, the system stabilizes into a hexagonal pattern, the orientation of which is arbitrary and may change from run to run. Therefore the situation that the symmetric ring pattern is unstable, while each "broken-symmetry" state of a hexagonal pattern is stable, is retained when one reduces the full 2D state space to the ring configuration.

Combining the simulation results in this section, using the full 2D, multi-$|\mathbf{k}|$, and ring models, one can see that an important class of transverse instability-driven patterns exist in a hexagonal state space. Moreover, a model including only the pump ($\mathbf{k} = \mathbf{0}$) mode and six modes on a regular hexagon (the single-hexagon model) would be sufficient to analyze the competitions and controlled switching among these patterns.

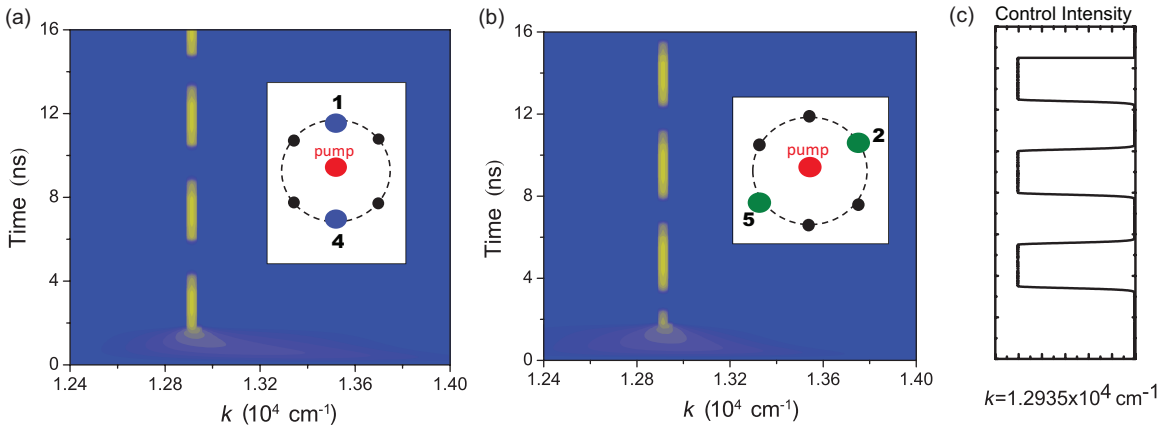

FIG. 7. (Color online) Radial distributions of reflected signal intensity in momentum space in directions 1 (a) and 2 (b) as functions of time. The intensity distributions in directions 4 and 5 are similar to those in 1 and 2, respectively. One radial mode always 'wins it all' at steady states. The insets indicate the positions of the winning modes in a transverse plane in the far field. (c) The temporal profile of the control beam. In this case, the control is directed in azimuthal direction 2 with a momentum magnitude matching that of the winning mode in direction 1.

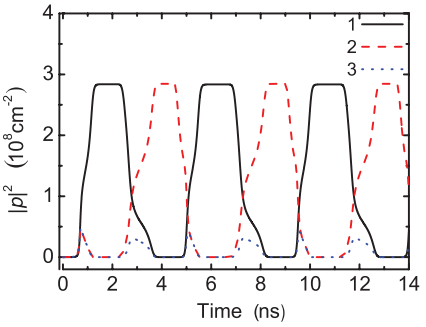

FIG. 8. (Color online) Exciton density for three off-axis directions in the single-hexagon model: $|p_1|^2$ is a black solid line, $|p_2|^2$ is a red dashed line, $|p_3|^2$ is a blue dotted line. Note that the dotted line, $|p_3|^2$, overlaps with the other lines over much of its range. The control beam, with peak intensity $\approx 3.6 \times 10^{-7} I_{\text{pump}}$ is first switched on at $t = 2$ ns in this run.

This analysis will be carried out in the following sections. Interactions among modes in different hexagons will be further studied in Sec. VIII. It will be seen that the insight gained from the single-hexagon model is also helpful in understanding these interhexagon competitions.

IV. SINGLE-HEXAGON MODEL

In this and the following three sections, the pattern dynamics in a hexagonal geometry are investigated in detail using the single-hexagon model. The results for our standard parameter values are reported in this section, and some parametric dependencies of the results are studied in Sec. V. Detailed analysis of the physical processes driving competition and control is contained in Secs. VI and VII.

The single-hexagon model includes only one sextuplet of points on the vertices of a hexagon plus the origin in $\mathbf{k}$ space, as illustrated in Fig. 5(c). Within the labeling scheme of the last two models we set the number of hexagons $N = 1$ and drop the index h. The momenta of the off-axis modes are written as $\mathbf{k}_i = k_r \hat{\mathbf{e}}_i, i = 1, \ldots, 6$, where, as in the ring model, k_r is assigned the value for the winning mode in the multi-$|\mathbf{k}|$ simulations. The field symbols are also simplified to p_i, E_i, $i = 0, \ldots, 6$, with $i = 0$ labeling the pump fields. Figures 8 and 9 show the simulation results using the same material and run-time parameters as in the multi-$|\mathbf{k}|$ simulation presented in the previous section. As in that simulation with the multi-$|\mathbf{k}|$ model, modes 1 and 4 are given a slight advantage, and a control beam is periodically applied to mode 2. Exciton densities in three off-axis directions, $|p_i|^2, i = 1,2,3$, are plotted as functions of time in Fig. 8. Their behaviors are clearly similar to those of the reflected light fields obtained within the multi-$|\mathbf{k}|$ model (see Fig. 6). In the winning off-axis direction, the steady-state exciton density is of the order of 10^8 cm^{-2}, or about 0.01 of the pump induced exciton density. While the rise time of p_1 in each cycle is about the same as in the multi-$|\mathbf{k}|$ model results, the time for complete switching, when the control is turned on, from direction 1 to 2, is roughly 200 ps longer here. As explained in the next section, a control intensity threshold for complete switching exists, and the longer switching time in the single-hexagon model indicates that this threshold is higher here than in the multi-$|\mathbf{k}|$ model.

Since the polariton scatterings represented in Eqs. (14) and (15) are coherent processes, the density transfer among modes depends critically on the relative phases of the fields involved. We display the phases of off-axis exciton fields relative to the pump's phase in Fig. 9. Their behaviors and their roles in the dynamics of pattern selection will be more thoroughly discussed in Secs. VI and VII below. The importance of phases was also investigated in other instability-driven structures, e.g., in Ref. 46.

The exciton density in the pump direction ($|p_0|^2$, which is not shown) reaches its peak value of about 10^{10} cm^{-2} at around $t = 30$ ps and stays constant except for a slight variation when the control is on. The phase of the pump exciton field also stays essentially constant at roughly 0.15π after $t = 30$ ps.

The pattern-formation time starting from the initial pump-only state varies with the models used. In general, this initial formation time is longer when there are more competing modes in the model, being shortest in the single-hexagon model and longest in the full 2D simulations. The switching time when the control beam is applied, however, is roughly the same in all models.

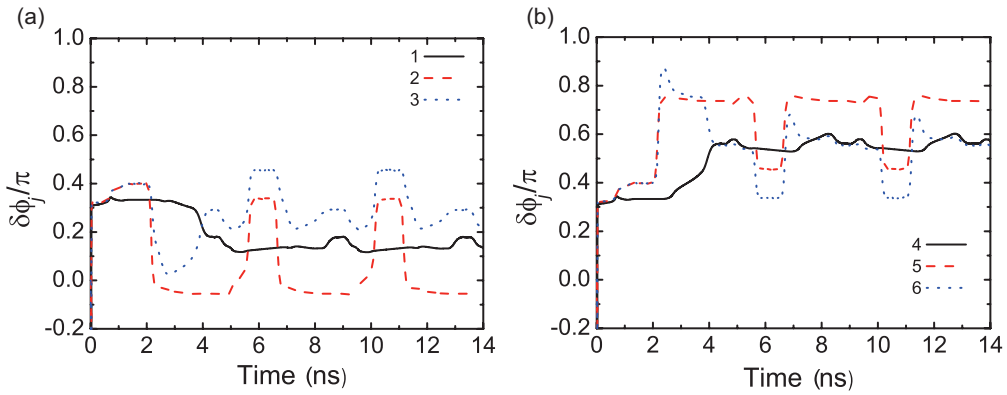

FIG. 9. (Color online) Phases of the exciton fields in the off-axis directions for the reference case within the single-hexagon model. (a) Phases in modes 1–3 and (b) phases in modes 4–6, relative to the pump-induced exciton phase, $\delta\phi_j = \phi_j - \phi_0, j = 1 - 6$. The modes are labeled in Fig. 5(c). Note that the symmetry between ϕ_j and ϕ_{j+3} is broken after the introduction of control beam at about $t = 2$ ns.

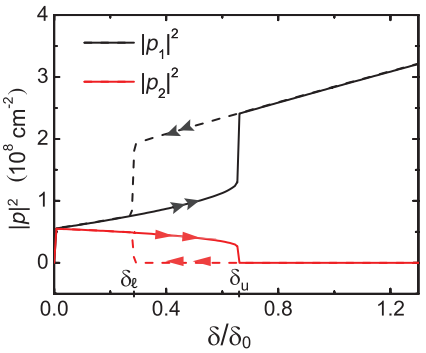

FIG. 10. (Color online) Steady-state exciton densities in directions 1 and 2 vs the amount of anisotropy—downward shift of the cavity mode energy in direction 1 (δ). $\delta_0 = 0.12$ meV is the shift in the reference case (see text). $|p_3|^2$(not shown) is equal to $|p_2|^2$. For $0 < \delta < \delta_\ell \approx 0.28\delta_0$, only the hexagonal pattern is stable. For $\delta > \delta_u \approx 0.66\delta_0$, only the two-spot (in modes 1 and 4) pattern is stable. Both patterns are stable in the range between δ_ℓ and δ_u, where their adiabatic evolutions show hysteresis behaviors: the solid (dashed) lines trace the evolution of the densities as δ increases (decreases) from small (large) values.

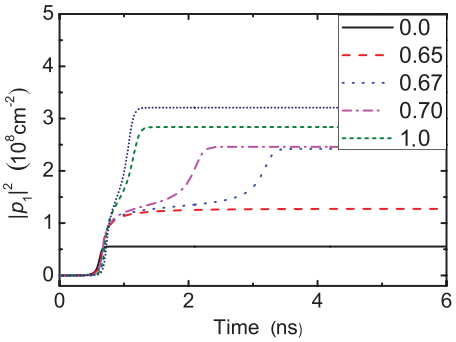

FIG. 11. (Color online) Exciton density in direction 1 (preferred direction) vs time for various amounts of downward shift in the cavity mode energy (δ) calculated in the single-hexagon model. The value of δ/δ_0 for each curve is given in the inset. For δ below, the critical value for hexagon-to-two-spot transition (see Fig. 10), $|p_1|$ attains steady state within 1 ns. For δ immediately above this critical value, e.g., the curve for $\delta/\delta_0 = 0.67$, $|p_1|$ passes through a long intermediate step before rising to its steady-state level.

V. PATTERN AND TIME SCALE VARIATIONS WITH PARAMETERS

In the previous two sections, we have discussed a particular scenario (with asymmetry applied) where a "two-spot" pattern is selected by the system's dynamics and then the pattern is rotated by a control beam. In this section, we investigate the range of stable patterns supported by the hexagonal state space and how the selection of patterns as well as the transition time between patterns depend on the system and control parameters. We will refer to the set of results presented in the previous section as the reference case.

A. Varying the anisotropy in the cavity mode energy

In the reference case, we introduced an anisotropy in the cavity mode energy $\omega^c_{\mathbf{k}}$ by down-shifting it by 0.12 meV in modes 1 and 4. We examine here the effects of changing the size of this anisotropy, which we denote by δ. The reference value of 0.12 meV is denoted by δ_0. Figure 10 shows the exciton densities in directions 1 and 2 in the steady state(s) as a function of δ/δ_0. The density in direction 3 is equal to that in direction 2 in each case. For $\delta = 0$, where there is complete symmetry among the six directions in the equations, we have found only the symmetric steady-state solution, with $|p_1| = |p_2| = |p_3|$, to be stable. (The equidensity hexagonal pattern is the "symmetric" state in the single-hexagon model. It is, however, a broken-symmetry state in the ring model where the symmetric state has density evenly distributed around the ring.) The hexagon remains the only stable pattern for values of δ between 0 and a lower critical value $\delta_\ell \approx 0.28\delta_0$, with the steady-state value of $|p_1|$ steadily growing while that of $|p_2| = |p_3|$ is falling. Between δ_ℓ and an upper critical value $\delta_u \approx 0.66\delta_0$, both the hexagon and the two-spot pattern, in directions 1 and 4, are stable. Above δ_u only the two-spot pattern is stable. In Fig. 10, the solid lines trace the evolution of the steady-state densities if δ is slowly increased from zero: they vary smoothly until δ crosses δ_u, when $|p_1|$ jumps up and $|p_2|$ (=$|p_3|$) drops abruptly to zero. Starting from large δ, when we decrease δ, the system follows the dashed lines inside the bistable range. The total off-axis density, summed over all six directions, increases with δ over the displayed range (not shown). For example, the total exciton density in the symmetric case ($\delta = 0$) amounts to about 50% of that in the reference case ($\delta = \delta_0$).

In Fig. 11, we compare the time evolution of $|p_1|^2$ for various values of δ during the transition from the initial vacuum state to the stable steady state. For this initial state, the system goes asymptotically to the hexagon steady state for values of δ in the bistable range. In each case, the pump intensity becomes practically constant at around $t = 30$ ps. The off-axis density becomes visible on the scale of the final steady-state level at about 0.6 ns. After this point, for $\delta < \delta_u$, $|p_1|^2$ takes a relatively short time—several tens of picoseconds—to reach its steady-state value. Beyond the hexagon-two-spot transition, however, the time trace of $|p_1|^2$ acquires an intermediate step, during which its change slows down, before its final rise to a constant value. The length of this intermediate step appears to increase without limit as δ approaches δ_u from above. Similar to the reference case, shown in Figs. 6 and 8, for each $\delta > \delta_u$, $|p_2(t)|^2$ and $|p_3(t)|^2$ stay nonzero during the time when $|p_1(t)|^2$ is passing through its intermediate step. Comparing the curves at $\delta = 0.65\delta_0$ and $0.67\delta_0$ suggests that the intermediate step is a "residual" effect of the hexagonal pattern. Though no longer a stable steady state, it still slows down the system's dynamics when the system passes through its vicinity. In cases not close to the hexagon-two-spot transition, one lower bound to the formation time of the stable pattern is the ps time scale of the electron-hole Hamiltonian. In most cases, the actual time scale is one to two orders of magnitude longer that this lower bound depending on the level of fluctuations and the balance between gain and (both radiative and nonradiative) loss rates.

When the asymmetry δ is set below 0, directions 1 and 4 are given a disadvantage, and the stable pattern is a hexagon with $|p_2|^2 = |p_3|^2 > |p_1|^2$. A transition to a four-spot pattern would not occur since the latter is not a steady-state solution to Eq. (15) (see Sec. VI below).

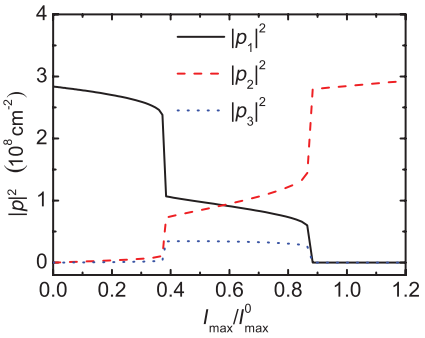

FIG. 12. (Color online) Steady-state exciton densities vs the peak intensity of a control beam introduced in direction 2. The control intensity (I_{max}) is expressed in units of that in the reference case, denoted here by I^0_{max}. As I_{max} increases, the pattern goes from two spots (in directions 1 and 4) through a hexagon to two rotated spots (in directions 2 and 5). A bistable region and attendant hysteresis behavior (not shown in the figure) are present at each abrupt transition.

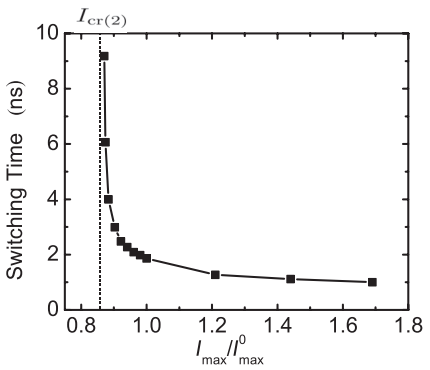

FIG. 13. Time taken to switch between a two-spot pattern in directions 1 and 4 to one in directions 2 and 5 vs the peak intensity of a control beam introduced in direction 2. The control intensity (I_{max}) is expressed in units of that in the reference case, denoted here by I^0_{max}.

The switching behavior of the hexagonal pattern for $\delta < \delta_u$ is similar to that in the reference case when the same control beam is applied. In the symmetric case ($\delta = 0$, for example), when the control beam is turned on in direction 2, the hexagon switches to the two-spot pattern with the density in directions 2 and 5 being the same as in the reference case. When the control beam is then turned off, the system goes back to the symmetric solution. The times needed for switching between the two patterns are slightly shorter than those in the reference case.

B. Varying the control beam intensity

In the reference case, a control beam with peak intensity $= 3.3 \times 10^{-2}$ W cm^{-2} $= 3.6 \times 10^{-7} I_{pump}$ is applied in direction 2. We examine here the effects of varying this control intensity, retaining for all other parameters their values as in the reference case. We denote the control intensity by I_{max} and its value in the reference case by I^0_{max}.

Figure 12 shows the steady-state exciton densities when the system is under irradiation by the control beam as functions of I_{max}. It can be seen that the pattern undergoes two abrupt changes. When the control is off ($I_{max} = 0$), the stable pattern has two spots in directions 1 and 4. As I_{max} increases from zero, $|p_1|^2$ ($=|p_4|^2$) falls, while $|p_2|^2$ ($\approx|p_5|^2$) and $|p_3|^2$ ($=|p_6|^2$) rise gradually. As I_{max} reaches a critical value $I_{cr(1)}$, which is between 0 and I^0_{max}, the hexagon with two bright spots and four dim spots changes abruptly to a hexagon with comparable brightness in all spots. Thereafter, $|p_1|^2$ continues to fall, while $|p_2|^2$ continues to grow until I_{max} reaches a second critical value $I_{cr(2)}$, which is $0.86 I^0_{max}$, where $|p_1|^2$ and $|p_3|^2$ drop to zero and the pattern changes abruptly to two spots in directions 2 and 5. Hence $I_{cr(2)}$ is the lowest control intensity that can completely switch the two spots from directions 1 and 4 to 2 and 5. Though not shown in Fig. 12, a bistable region and hysteresis behavior, similar to those in Fig. 10, are present at each abrupt transition.

The time traces of the densities in the reference case, in Figs. 6 and 8, show intermediate steps also during the switching process. As in the initial pattern formation stage, the intermediate step here can be interpreted as a "transient trapping" of the system in the vicinity of the hexagonal state that loses its stability at $I_{max} = I_{cr(2)}$. The duration of this intermediate step also becomes longer as we set the control intensity closer to the critical value $I_{cr(2)}$. For I_{max} sufficiently close to $I_{cr(2)}$, the time the system spends in this transient trapping dominates the time taken by the two-spot pattern to switch directions. Illustrating this, we plot the switching time as a function of I_{max} in Fig. 13. Again, there does not appear to be an upper bound to this duration. Away from $I_{cr(2)}$ when the system is no longer affected by the hexagonal state, the switching time is around 1ns.

If the asymmetry δ is decreased, the critical control intensity for rotating the two-spot pattern $I_{cr(2)}$ is also lowered. However, as there is a minimum value for δ, namely δ_{cr} for the two-point solution to be stable, a lower bound to the switching intensity exists for a fixed set of material parameters and pump intensity.

VI. DYNAMICAL ANALYSIS

In the following two sections, we seek to gain insight into the physical mechanisms underlying the phenomena of pattern formation and switching displayed in the previous sections. For this purpose, we analyze the interplay between the various wave mixing (or coherent scattering) processes contributing to the polariton dynamics. To keep the discussion most transparent, we will work within the single-hexagon model.

It is convenient to break the complex fields in the rotating frame down to their magnitudes and phases and consider the equations of motion for these components:

$$p_j = \tilde{p}_j e^{-i\phi_j}, \quad E_j = \tilde{E}_j e^{-i(\phi_j - \xi_j)}, \tag{16}$$

for $j = 0, \ldots, 6$. Here, ξ_j is defined to be the phase difference between the exciton field p_j and the cavity photon field E_j. Substituting Eq. (16) into Eqs. (14) and (15), we get for the off-axis fields ($j = 1, \ldots, 6$),

$$\frac{d\tilde{p}_j}{dt} = \frac{1}{\hbar \tilde{p}_j} \mathrm{Im}(i\hbar \dot{p}_j p_j^*) = L_{p_j} + Q_{p_j} + C_{p_j}, \tag{17}$$

$$\frac{d\phi_j}{dt} = \frac{1}{\hbar \tilde{p}_j^2} \mathrm{Re}(i\hbar \dot{p}_j p_j^*) = \frac{1}{\tilde{p}_j}\left(L_{\phi_j} + Q_{\phi_j} + C_{\phi_j}\right), \tag{18}$$

where

$$\hbar L_{p_j} = V_{\mathrm{HF}}\tilde{p}_{j+3}\tilde{p}_0^2 \sin\left(\Phi_{j,j+3}^{0,0}\right) + 2\tilde{A}\Omega\tilde{p}_0\tilde{E}_0\tilde{p}_{j+3}\sin\left(\Phi_{j,j+3,\xi_0}^{0,0}\right) - \Omega\tilde{E}_j\sin(\xi_j)\left(1-2\tilde{A}\tilde{p}_0^2\right) + 2\tilde{A}\Omega\tilde{p}_0\tilde{E}_0\tilde{p}_j\sin(\xi_0) - \gamma_x\tilde{p}_j, \tag{19}$$

$$\begin{aligned}\hbar Q_{p_j} = {} & 2\tilde{p}_{j-2}\left[V_{\mathrm{HF}}\tilde{p}_0\tilde{p}_{j-1}\sin\left(\Phi_{j,j-2}^{0,j-1}\right) + \tilde{A}\Omega\tilde{E}_0\tilde{p}_{j-1}\sin\left(\Phi_{j,j-2,\xi_0}^{0,j-1}\right) + \tilde{A}\Omega\tilde{p}_0\tilde{E}_{j-1}\sin\left(\Phi_{j,j-2,\xi_{j-1}}^{0,j-1}\right)\right] \\ & + 2\tilde{p}_{j+2}\left[V_{\mathrm{HF}}\tilde{p}_0\tilde{p}_{j+1}\sin\left(\Phi_{j,j+2}^{0,j+1}\right) + \tilde{A}\Omega\tilde{E}_0\tilde{p}_{j+1}\sin\left(\Phi_{j,j+2,\xi_0}^{0,j+1}\right) + \tilde{A}\Omega\tilde{p}_0\tilde{E}_{j+1}\sin\left(\Phi_{j,j+2,\xi_{j+1}}^{0,j+1}\right)\right] \\ & + 2\tilde{p}_0\left[V_{\mathrm{HF}}\tilde{p}_{j+1}\tilde{p}_{j-1}\sin\left(\Phi_{j,0}^{j+1,j-1}\right) + \tilde{A}\Omega\tilde{E}_{j+1}\tilde{p}_{j-1}\sin\left(\Phi_{j,0,\xi_{j+1}}^{j+1,j-1}\right) + \tilde{A}\Omega\tilde{p}_{j+1}\tilde{E}_{j-1}\sin\left(\Phi_{j,0,\xi_{j-1}}^{j+1,j-1}\right)\right],\end{aligned} \tag{20}$$

$$\begin{aligned}\hbar C_{p_j} = {} & 2V_{\mathrm{HF}}\tilde{p}_{j+3}\left[\tilde{p}_{j+1}\tilde{p}_{j-2}\sin\left(\Phi_{j,j+3}^{j+1,j-2}\right) + \tilde{p}_{j+2}\tilde{p}_{j-1}\sin\left(\Phi_{j,j+3}^{j+2,j-1}\right)\right] + 2\tilde{A}\Omega\tilde{p}_{j+3}\sum_{i\neq j,j+3}\tilde{p}_i\tilde{E}_{i+3}\sin\left(\Phi_{j,j+3,\xi_{i+3}}^{i,i+3}\right) \\ & + 2\tilde{A}\Omega\tilde{E}_j\sin(\xi_j)\sum_i\tilde{p}_i^2 + 2\tilde{A}\Omega\tilde{p}_j\sum_{i\neq j}\tilde{p}_i\tilde{E}_i\sin(\xi_i),\end{aligned} \tag{21}$$

and

$$\begin{aligned}\hbar L_{\phi_j} = {} & \left(\varepsilon_{h,j}^x - \hbar\omega_p + V_{\mathrm{HF}}\tilde{p}_0^2\right)\tilde{p}_j + V_{\mathrm{HF}}\tilde{p}_{j+3}\tilde{p}_0^2\cos\left(\Phi_{j,j+3}^{0,0}\right) + 2\tilde{A}\Omega\tilde{p}_0\tilde{E}_0\tilde{p}_{j+3}\cos\left(\Phi_{j,j+3,\xi_0}^{0,0}\right) \\ & - \Omega\tilde{E}_j\cos(\xi_j)\left(1-2\tilde{A}\tilde{p}_0^2\right) + 2\tilde{A}\Omega\tilde{p}_0\tilde{E}_0\cos(\xi_0)\tilde{p}_j,\end{aligned} \tag{22}$$

$$\hbar Q_{\phi_j} = \hbar Q_{p_j}[\sin\mapsto\cos], \tag{23}$$

$$\hbar C_{\phi_j} = \hbar C_{p_j}[\sin\mapsto\cos] + V_{\mathrm{HF}}\tilde{p}_j\left(2\sum_{i\neq j}\tilde{p}_i^2 + \tilde{p}_j^2\right), \tag{24}$$

where $\Phi_{i,j}^{l,m} = \phi_i + \phi_j - \phi_l - \phi_m$ and $\Phi_{i,j,\xi_k}^{l,m} = \phi_i + \phi_j + \xi_k - \phi_l - \phi_m$. In these equations, each sum over i ranges from 1 to 6. In Eqs. (23) and (24), a function followed by the symbol $[\sin\mapsto\cos]$ means the same function with all sines replaced by cosines in its expression. We have grouped the contributing terms according to their order in the off-axis fields. As the symbols imply, L_{p_j}, Q_{p_j}, and C_{p_j} contain respectively first (linear), second (quadratic), and third-order (cubic) terms in p_j or E_j, $j = 1,\ldots,6$. The same applies to L_{ϕ_j}, Q_{ϕ_j}, and C_{ϕ_j}. The state with polariton density only in the pump mode is treated as the zeroth-order state. The pump fields p_0 and E_0 experience very small (fractional) changes in time and will be taken approximately as constant in this analysis.

As mentioned before, all exciton interactions and PSF terms can be visualized as either a four-wave mixing process with wave-vector matching or a polariton-polariton scattering process with momentum conservation. For each scattering process in Eqs. (14) and (15), the exciton field on the left-hand side and the conjugated field on the right-hand side are in the outgoing modes while the other two fields on the right-hand side are in the incoming modes. Of course these scatterings are coherent, not of the Boltzmann, mass-action type: the direction of density transfer depends on the interference between the scattered wave and the existing field in each outgoing channel. In Eqs. (17)–(24), the phases of the incoming fields are subtracted from those of the outgoing fields inside the sine or cosine functions. Since the density equations contain the sine functions, the term is a gain term for the mode in question if the combined phases of the outgoing fields lead (by less than π) those of the incoming fields. Otherwise, it is a loss term. For the phase's rate of change, with the cosine functions, a process tends to increase the phase in question if the phase difference between the outgoing fields and the incoming fields is less than $\pi/2$.

The first two terms contributing to L_{p_j} in Eq. (19) are the primary instability-driving (gain) processes, in which two pump polaritons scatter off each other into two opposite off-axis directions. An example is displayed pictorially in Fig. 14(a). The next term is the exciton-photon coupling in an off-axis mode, partially blocked by the pump exciton density. In the calculations, the angle ξ_j is always positive, corresponding to an expected net energy flow from the exciton field $\tilde{p}_j$ to the photon field $\tilde{E}_j$. Hence, to the exciton field, this term represents the radiative loss from mode $\mathbf{k}_j$. The next term describes the forward scattering between a pump photon and an off-axis exciton, or equivalently, a self-wave mixing process in which a pump photon scatters off a density grating, set up by the pump and the off-axis exciton fields, into the off-axis direction. In the pump mode, energy flows on balance from the cavity photon field to the exciton field, resulting in a negative phase-lag angle ξ_0. Hence this scattering actually results in a density transfer from the off-axis $\mathbf{k}_j$ mode to the pump mode. The last term $-\gamma_x\tilde{p}_j$ represents all nonradiative losses. The balance between gain and loss terms determines the sign and magnitude of L_{p_j}.

In a quadratic process, i.e., one that contributes to Q_{p_j} and Q_{ϕ_j}, one off-axis polariton (from mode $\mathbf{k}_j$) and a pump polariton scatter into the modes $\mathbf{k}_{j-1}$ and $\mathbf{k}_{j+1}$ and vice

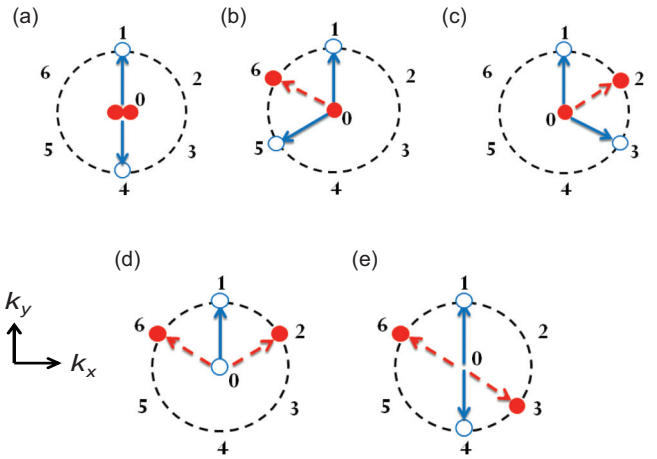

FIG. 14. (Color online) Pictorial representations of polariton scattering processes contributing to the equation of motion of p_1. The processes are (a) linear, (b)–(d) quadratic, and (e) cubic in the off-axis fields. In each diagram, the incoming modes and outgoing modes in the scattering are labeled by red, solid circles and blue, open circles, respectively. The arrows represent the modes momenta, dashed (solid) for the incoming (outgoing) modes. For example in (b), two polaritons from directions 0 (pump) and 6 scatter into directions 1 and 5.

versa. These processes are also illustrated in Fig. 14: the first three terms in Eq. (20) are represented by Fig. 14(b), the next three terms by Fig. 14(c), and the last three terms by Fig. 14(d). We note that the momentum conservation condition that gives rise to the quadratic terms is satisfied only for modes arranged geometrically in a hexagon. Among the cubic terms, the first three contributing to C_{p_j} and C_{ϕ_j} represent two counter-directed polaritons on the hexagon scatter into a different pair of opposite directions. An example is drawn in Fig. 14(e). The next two terms are, respectively, the Pauli blocking reduction of the (linear) exciton-photon coupling by the exciton density in all off-axis modes and a self-wave-mixing process in which a photon in mode i ($i \neq j$) scatters off a density grating, set up by p_i and p_j, into mode j. Since $0 < \xi_i < \pi/2$ for $i = 1, \ldots, 6$, these two terms are positive in both Eqs. (21) and (24). The last term contributing to C_{ϕ_j} in Eq. (24) is a (blue) shift in frequency for p_j. In contrast to the quadratic terms discussed above, these cubic processes do not require a hexagon mode configuration to be operative.

We finally note a phase degeneracy in the solution to Eqs. (17)–(24). Suppose $(\tilde{p}_j(t), \phi_j(t)), j = 1, \ldots, 6$ is a solution to these equations. Then one can verify that $(\tilde{p}_j(t), \phi_j(t) + \delta\phi_j)$ is also a solution provided the six $\delta\phi_j$'s are time independent and satisfy the following constraints:

$$\delta\phi_j + \delta\phi_{j+3} = 2\pi m, \tag{25}$$

$$\delta\phi_{j+1} + \delta\phi_{j-1} - \delta\phi_j = 2\pi m, \tag{26}$$

where m is an integer, and the subscript is again counted cyclically through 1 to 6. These two constraints restrict the number of undetermined phases to two. This applies, in particular, to steady-state solutions. Thus there exist an infinite number of steady-state solutions to Eqs. (17)–(24), which can be grouped into a finite number of classes. The solutions in each class have the same set of magnitudes and are parameterized by two free phases. We see an example of this phase freedom in Fig. 9, when we compare the phases of, say, p_1 and p_4 during the initial steady state with their phases when the system returns to the (1,4) two-dot pattern after the first on/off switching cycle. The individual steady-state phases are different in the two time periods, while their sum stays the same. Therefore, strictly speaking, the system "returns" after the on/off switching cycle to a different steady state that has the same set of magnitudes as before. Put another way, in a hypothetical experiment, the measured relative phase between E_1 and E_0 may be affected by uncontrollable factors, but the measured average phase of E_1 and E_4 relative to E_0's phase can be meaningfully compared to our theory's prediction.

VII. INTERPLAY OF WAVE MIXING PROCESSES

We now discuss the contributions and interplay of the various processes in effecting pattern selection and switching in the reference case (see Sec. IV). As could be expected, pattern competition in even the single-hexagon model is the result of rather complex, activating or inhibiting, feedbacks among these processes. Not being simply additive, their effects are not easy to disentangle cleanly. Nevertheless, as we show below, very useful insights could be gained by characterizing whether each process is activating or inhibiting to each mode's density. It is clear from Eqs. (19)–(21) that to understand how the exciton densities evolve, one needs information on the relative phases of the polariton fields involved in the scatterings. The calculated magnitudes and phases of the off-axis p_j for the reference case were plotted in Figs. 8 and 9. Figure 15 shows the contributions of the three groups of terms—linear, quadratic, and cubic—to the rates of change of the exciton densities in directions 1 and 2, and Fig. 16 shows these contributions to the evolution of the respective exciton phases.

1. Linear contributions

Initially, the linear terms dominate, and in each off-axis mode, the exciton phase ϕ_j is quickly locked into a value given by the solution of $d\phi_j/dt \approx L_{\phi_j}/\tilde{p}_j = 0$, where L_{ϕ_j} is given by Eq. (22). Actually, as explained above, this condition fixes only the value of the sum $\phi_j + \phi_{j+3}$ but not either phase angle individually. In the calculations, however, all the exciton phases are initially set at 0, and since $L_{\phi_j}/\tilde{p}_j \approx L_{\phi_{j+3}}/\tilde{p}_{j+3}$, we also have $\phi_j \approx \phi_{j+3}$ in the linear regime. The radial $|\mathbf{k}|$ value of the off-axis modes having been chosen optimal, we have [cf. Eq. (19)]

$$\Phi^{0,0}_{j,j+3} = \phi_j + \phi_{j+3} - 2\phi_0 \approx \pi/2. \tag{27}$$

In Fig. 9, this phase lead is about 0.6π for each of the three off-axis mode pairs. Once their phases are locked, the off-axis exciton densities grow exponentially from fluctuation levels. We are considering pump intensities close to the phase-conjugate instability threshold. This condition implies a substantial cancellation between the gain and loss terms in L_{p_j}. In the reference case calculations, the exponential off-axis growth rate in the first 0.6 ns is about 0.01 ps^{-1}, which is much

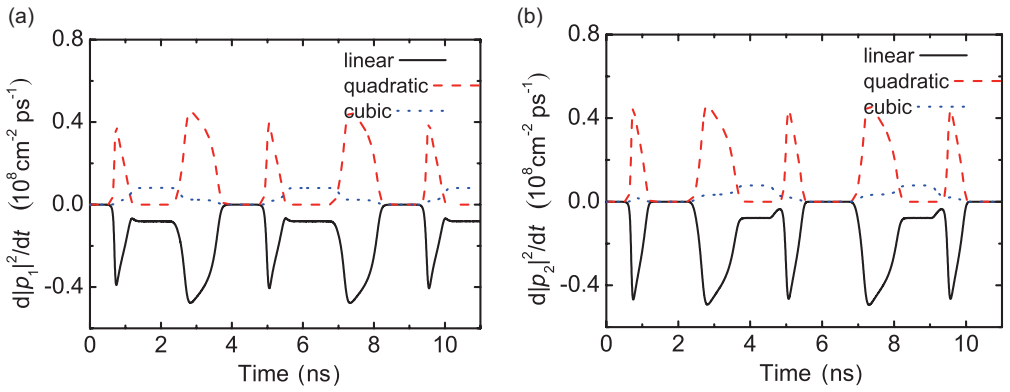

FIG. 15. (Color online) Contributions of the linear, quadratic, and cubic terms to the rate of change of exciton densities in directions 1 (a) and 2 (b) in the reference case.

slower than the typical inverse time scales given by the exciton Hamiltonian (e.g., $\gamma_x/\hbar = 0.67\ \mathrm{ps}^{-1}$). During this exponential growth phase, the $\tilde{p}_j$'s are actually too small to be visible on the scale in Fig. 8. It is interesting to note that, although the asymmetry-favored p_1 (and p_4) eventually wins out at the steady state, p_2 actually grows slightly faster than p_1 during the initial 0.6 ns. Thus the asymmetry confers its advantage through the quadratic and/or cubic processes. Put another way, the selection of (p_1, p_4) as the winning directions by the asymmetry works through the interactions among excitons in all six off-axis directions.

2. *Quadratic contributions*

The linear growth regime lasts approximately 0.5 ns. As the $\tilde{p}_j$'s grow, the quadratic and cubic contributions to dp_j/dt come into play. The onset of the quadratic terms has two effects. First, their *direct* contribution to the magnitude equation, Q_{p_j} in Eqs. (17) and (20), is positive, as shown in Fig. 15. This can be understood as follows. As explained in Sec. VI, whether a scattering term is a gain or loss process depends on the phase sum of the outgoing exciton-polariton fields relative to that of the incoming fields. In each term contributing to Q_{p_j}, one of the four exciton fields is in the pump mode while the other three are off-axis. As we have seen above in Eq. (27), the linear instability sets up the off-axis fields with phases leading the pump's by a large margin. In the first six terms of Eq. (20), represented by Figs. 14(b) and 14(c), p_0 is among the incoming fields, and thus the relative phase angles are typically positive (between 0 and π). These six terms are therefore gain terms. The photon/exciton phase shift in each mode, ξ_j, is very small and its effect can be ignored in this argument. In contrast, the last three terms in Eq. (20), represented by Fig. 14(d), yield losses because p_0 is outgoing in them. Since the three triplets of terms are roughly equal in magnitude, and the gains outnumber the losses, the net result for Q_{p_j} is typically positive.

The second effect of the quadratic terms acts through their contributions to $d\phi_j/dt$ in Eq. (18). Again from the linear phase lead, Eq. (27), one can deduce that the relative phases in the terms contributing to Q_{ϕ_j} in Eq. (23) typically lie, during the onset of the quadratic terms, between $-\pi/2$ and $\pi/2$, Q_{ϕ_j} is therefore positive, as shown in Fig. 16. The resulting increase in ϕ_j exerts a negative feedback effect on the linear scattering process in L_{p_j}: since the relative phase in the linear gain terms $\sin(\Phi^{0,0}_{j,j+3})$ is a little over $\pi/2$ during the initial growth period, pushing ϕ_j (and ϕ_j+3) up reduces the gain, and since the loss terms, e.g., $\gamma_x\tilde{p}_j$, are not affected, L_{p_j} suffers a net decrease and becomes negative, as can be seen in Fig. 15. In fact, the

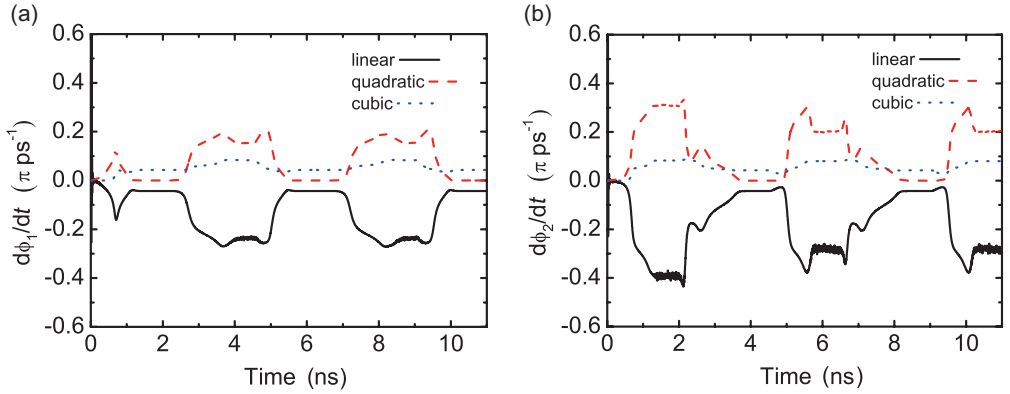

FIG. 16. (Color online) Contributions of the linear, quadratic, and cubic terms to the rate of change of exciton phases in directions 1 (a) and 2 (b) in the reference case.

upsurge of $\tilde{p}_{1/4}$ to their winning (two-spot) steady state is associated with a slower rise in $\phi_{1/4}$ than in the other modes' phases. Initially locked at zero, L_{ϕ_j} is also decreased by the growing $\Phi^{0,0}_{j,j+3}$ negative values, as shown in Fig. 16, thus offsetting the effects of Q_{ϕ_j} to some degree.

3. Cubic contributions

The contributions of the third-order scattering processes to the exciton density, i.e., the first three terms in Eq. (21), depend on the relative phases between the off-axis fields. When $\tilde{p}_1$ is winning, since $\phi_1 < \phi_2 = \phi_3$, inspecting Eq. (21) shows that these terms are negative for C_{p_1} and positive for C_{p_2} and C_{p_3}, or they tend to equalize the densities in the six modes. The remaining two terms in C_{p_j} are Pauli blocking terms that reduce the flow of density from p_j to E_j and so are gain terms to mode j. In the two-spot steady state with modes 1 and 4, the only surviving contribution to C_{p_1} is $2\tilde{A}\Omega\tilde{E}_1\tilde{p}_1^2\sin(\xi_1)$. Similar to Q_{ϕ_j}, all terms in C_{ϕ_j} in Eq. (24) are positive, thus again helping to lower the linear amplitude term L_{p_1}. The first set of terms in Eq. (24) again represent coherent scatterings and Pauli blocking. The last term is a blue shift of the exciton energy in mode j due to interactions with off-axis excitons.

4. Role of quadratic processes in stabilizing hexagon

It is instructive to consider an artificial reduction of the single-hexagon model in which the quadratic processes are disabled. In this case, the most basic function of the cubic processes is to saturate the polariton density in the off-axis modes, which the cubic processes achieve mostly through raising the phases of p_j's, as explained above. Setting the quadratic terms [last three lines in the single-hexagon of Eq. (15), or equivalently, Q_{p_j} and Q_{ϕ_j} in Eqs. (17) and (18)] to zero, we have repeated the simulations with the same parameters as in the runs shown in Sec. V. Figure 17 shows the exciton densities in modes 1 to 3 for an isotropic setting, i.e. no advantage is given to modes 1 and 4 ($\delta = 0$). Unlike the "physical" case, with the quadratic terms operative, where

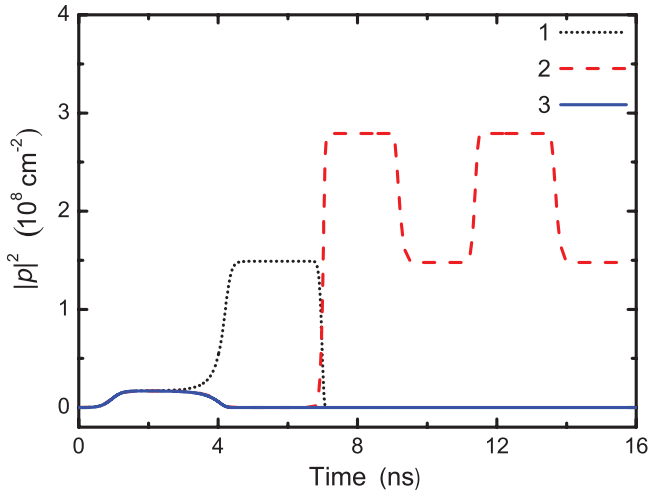

FIG. 17. (Color online) Exciton densities in directions 1 to 3 for the reference case but with the quadratic terms disabled and no asymmetry in the cavity dispersion relation. The first on/off cycle of the control beam starts at $t = 7$ ns.

the symmetric hexagon pattern is stable, the stable steady state in Fig. 17 is a two-spot pattern—the sixfold symmetry of the single-hexagon model is spontaneously broken. Which pair of modes win at the expense of the others is not determined by the model's physics and changes from run to run. When a sufficiently strong control beam is applied to mode 2, the pattern switches over to modes 2 and 5, but stays in this pair when the control is turned off. This is consistent with the fact that, in the isotropic setting, the two-spot pattern at modes 2 and 5 is the stable state closest to the steady state maintained by the control beam.

It is useful here to draw some insight from previous analyses of other multiple-mode competition models[47–49] that are based on linear growth and cubic saturation. Consider Lamb's two-mode laser model,[47] where each mode exerts a cubic saturation effect on both itself and the other mode. For this model, a symmetric steady state, with equal intensity in the two modes, is stable if self-saturation is more efficient than cross-saturation, while two asymmetric states, each with intensity in only one mode, are stable if cross-saturation is more efficient. By analogy, we also subdivide the contributions to C_{ϕ_j} and C_{p_j} into those due to densities in modes in j and $j+3$ and those due to densities in other modes, and refer to the two classes as self-saturating and cross-saturating contributions, respectively. The analogy is not exact because the effects of the two classes on $d\tilde{p}_j/dt$ are not simply additive, as their counterparts in Lamb's model[47] are, but these arguments are still applicable qualitatively, and our numerical results indicate that the cross-saturation cubic processes in our model polariton system are more efficient than the self-saturation processes. We have already seen that turning the quadratic processes back on in the isotropic setting destabilizes the two-spot pattern, while restoring stability to the symmetric hexagonal pattern. This indicates that the enhancement brought by Q_{p_j} to $d\tilde{p}_j/dt$ outweighs the suppression caused by the positive Q_{ϕ_j} in raising the phase of p_j. Thus the net effect of the quadratic processes can be classified as "cross-activating." The introduction of anisotropy ($\delta > 0$) modifies the balance of the above activating and saturating effects and, when strong enough, destabilizes the hexagonal pattern.

In the above, we have analyzed the physical processes driving transverse pattern selection and control in a quantum well microcavity and attempted to pursue a semi-phenomenological analogy between the pattern dynamics in this system and other mode-(or pattern-)competition systems. We will explore this analogy further in a future publication.

VIII. COMPETITIONS AMONG HEXAGONS

With the single-hexagon model, we have analyzed the switching between patterns that are the subsets of the same (regular) hexagon. In this section, we investigate switching between patterns that reside in different hexagons, as displayed in simulations using the multi-$|\mathbf{k}|$ and ring models. One can see by inspecting Eq. (15) that the quadratic processes [last three lines of Eqs. (15)] take place only among modes situated on the same hexagon. Modes on different hexagons compete with each other only through the cubic processes. From the intuition that we formed in the previous section that cubic cross-saturation in our system is more efficient than

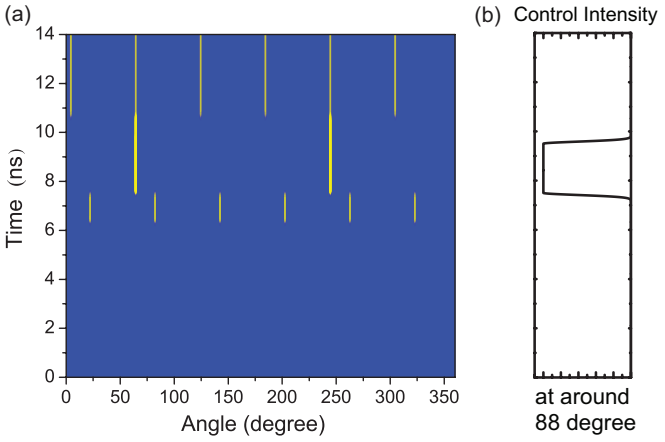

FIG. 18. (Color online) (a) Time evolution of the angular distribution of the reflected signal intensity in momentum space, calculated in the ring model. Although the setup is perfectly isotropic, the ring pattern is unstable while the hexagons are stable. The orientation of the hexagonal pattern obtained in each run is arbitrary. A control beam is introduced at $t = 7$ ns, directed at a mode outside of the initial hexagon, switching the pattern to a two-spot one. When the control beam is switched off at $t = 9.5$ ns, the signals form a hexagon in the orientation defined by the control beam. (b) Temporal profile of the control beam intensity.

self-saturation, we expect patterns that break the symmetry *among* hexagons to be favored. We have already seen that this is consistent with the simulation results in the 2D **r**-space model and the ring model in Sec. III. In both simulations, the setup is isotropic, but a hexagon pattern with arbitrary orientation is stable while the ring pattern is not. Within the hexagon, the cross-activating quadratic processes stabilize the symmetric hexagonal pattern at the expense of the two-spot solutions. In Fig. 18, we show some extended results of the ring model simulation. The figure shows the time evolution of the angular distribution of intensity. Starting with only the pump mode, the system forms a hexagon at about $t \approx 6.5$ ns, and the exciton density in the winning hexagon is 5.6×10^7 cm^{-2}, which is the same as the steady-state density in the symmetric multi-$|\mathbf{k}|$ model (not shown). A control beam with the same intensity as the one in the reference case is applied to another mode on the ring. Just as in the reference case, the control stabilizes a two-spot pattern with one spot in the mode it shines on. When the control beam is subsequently turned off, the off-axis pattern reverts to a hexagon that is oriented to contain the previous two-spot pattern as a subset. This is again consistent with the fact that each individual hexagon pattern is stable, and when the two-spot pattern is rendered unstable by the control beam's removal, the system settles into the nearest stable pattern.

A comparable situation is present in the multi-$|\mathbf{k}|$ simulations. We performed a simulation similar to the one shown in Figs. 6 and 7 except that the control beam is applied to a mode on a different hexagon (i.e., having a different radial momentum $|\mathbf{k}|$) from the initial two-spot pattern. Recall the notations in Sec. III: with the anisotropy-induced preference, the initial two-spot pattern is in modes $\mathbf{k}_{h_0,1}$ and $\mathbf{k}_{h_0,4}$, and the control beam is applied to mode $\mathbf{k}_{h_0,2}$. Here, the control is directed at mode $\mathbf{k}_{h_0',2}$ with h_0' being a close neighbor of h_0. Figure 19 shows the time evolution of the exciton density in modes over a range of h, or $|\mathbf{k}|$, values in directions 1 and 2. One can see that when the control is on, the pattern follows it to the mode pair $\mathbf{k}_{h_0',2}$ and $\mathbf{k}_{h_0',5}$. When the control is turned off, the pattern switches back to directions 1 and 4 but stays in the radial momentum mode set by the control, i.e., to the modes $\mathbf{k}_{h_0',i}, i = 1,4$ instead of the original $\mathbf{k}_{h_0,i}, i = 1,4$. In subsequent cycles of switching, the pattern stays in the hexagon defined by h_0'. These behaviors again indicate that, in the absence of the control, there exist a group of stable steady states, in each one of which the signal is concentrated in a mode with $\mathbf{k} = \mathbf{k}_{h,i}, i = 1,4$ and h is within a certain range about h_0. Which state the system evolves into depends on the system's history, e.g., which mode the signal is in when the control is turned off. In contrast to the situation in the ring model, however, there is no symmetry under which these modes are equivalent, for example, they have different single-polariton energies.

IX. SUMMARY AND OUTLOOK

In this paper, we have studied the nonlinear polariton dynamics of a laser-pumped quantum well microcavity as a

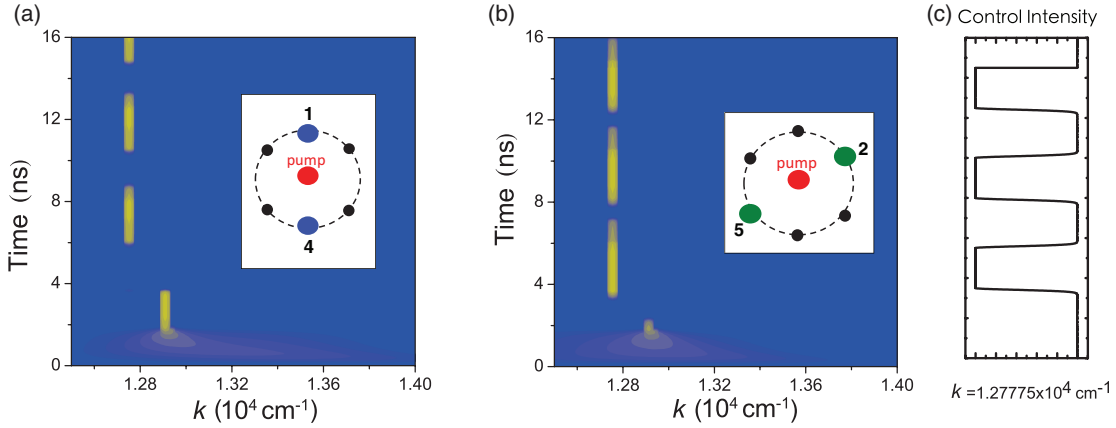

FIG. 19. (Color online) Time evolution of the radial distributions of reflected signal intensity in momentum space in directions 1 (a) and 2 (b), calculated in the multi-$|\mathbf{k}|$ model. One radial mode always "wins it all" at steady state. The inset in each panel indicates the positions of the winning modes in a transverse plane in the far field. (c) Temporal profile of the control beam. In this case, the control is directed in azimuthal direction 2 with a momentum magnitude smaller than that of the winning mode in direction 1.

spontaneous pattern-forming system. Using a microscopic theory of exciton-exciton interactions and GaAs parameters, we have examined the formation, selection, and control of the various transverse polariton density modulation patterns. We have analyzed in detail the polariton scattering processes that govern the competitions among patterns, obtaining useful insights into the crucial role played by the (relative) phases of the polariton amplitudes in driving the gains and losses of the densities in various **k** modes. We have also performed a more comprehensive investigation of a previously proposed low-intensity, all-optical switching scheme[8] that exploits these patterns.

One outcome of our analysis is a qualitative characterization of the effects of the various scattering processes in terms of notions used in discussing pattern formation and competition in other, usually classical, physical systems. These notions are based only on the polariton densities, despite the fact that the competitions among polariton amplitudes acts to an important extent through their phases. This has helped us form an intuitive picture of the pattern dynamics in our polariton system. We have pursued this analogy with other pattern-forming systems further and have constructed a three-state mode-competition model, which can be related to our models here and whose dynamics mimic almost all the qualitative behaviors displayed so far by the solutions of the single-hexagon model. Because of its simplicity, this mode-competition model is amenable to semi-analytic treatment, and we have obtained a complete classification of the steady-state solutions in the relevant region of parameter space. This "global" perspective introduces a useful organizational framework to discuss the qualitative dynamics of our system. This work will be reported in a future publication.

An actual quantum well microcavity sample may contain static structural disorder in both the mirrors and the quantum wells, caused by, e.g., interface roughness, crystal structure mismatch, and dislocations (e.g., Ref. 45). In this paper, we have not considered how these disorders affect the pattern dynamics. We briefly comment on some of their expected effects here. Static disorders in quantum wells have been studied, for example, in Ref. 50. When embedded in microcavities, these disorders break the translational and rotational symmetries in the transverse plane, leading to (multiple) scattering of polaritons. Their effects on the properties of polariton condensates[51] and as probes of the superfluidity of polaritons[52] have been discussed. One optical signature of disorder in microcavities is resonant Rayleigh scattering (RRS) of polaritons, which has been found[53] to produce rings (on a picosecond time scale) in the planar **k** space from a uniform pump-induced polariton field at pump intensities below the threshold for directional instabilities. Compared to specular reflection, the RRS signal was found to be four to five orders of magnitude weaker. With regard to the pattern formation that we have discussed in this paper, it may be conjectured that, under disorder conditions similar to those of Ref. 53, RRS serves as one mechanism (among others) to produce seed fluctuations in the polariton field that initiate instability growth at finite **k**. For weak disorders, RRS is not expected to alter drastically the dynamics of pattern formation and competition that we have analyzed in this paper. This condition appears to be obtained in the recent demonstration of patterns in Ref. 17. Nevertheless, it will be interesting to further study the effects of disorder in the future. This could include the possibility of strongly anisotropic disorders (for example, those attributed to disorder in the Bragg mirrors[45,53]), which could be related to the anisotropy parameter in our model, the effects of which were studied in Sec. V.

ACKNOWLEDGMENTS

The Paderborn group acknowledges financial support from the DFG and a grant for computing time at PC^2 Paderborn Center for Parallel Computing. The CUHK group thanks the assistance and the computing facilities available from the Research Computing Team at The Chinese University of Hong Kong. N.H.K. acknowledges financial support from the Center of Optical Sciences of the Chinese University of Hong Kong. We also thank J. Lega, T. Y. Tsang, and K. P. Chan for very helpful discussions.

APPENDIX: COUPLING BETWEEN THE CAVITY MODES AND MACROSCOPIC FIELDS

In this Appendix, we give more details on our model for the coupling between the macroscopic light field and the cavity modes. The relations (5) and (6) between input and output fields will be derived, and the choice of Eq. (7) will be given support by showing it leads to the interpretation of the cavity field magnitude squared $|E_{\mathbf{k}}|^2$ as a photon density. In our model, the cavity modes are taken to be the spatial Fourier modes of an oscillator field separate from the macroscopic light field and confined to an infinitely thin plane. The QW is assumed to be embedded inside this planar cavity, and the oscillator field and the exciton field are coupled to form the polariton field. The (linear) coupling between the cavity oscillator field and the outside radiation field is modeled like the coupling between the latter and a material oscillator field. Since all macroscopic light modes involved are near-normal (deviations of their wave vectors from the normal direction are typically less than 10°), for simplicity, the complications due to the finite polar angles of the off-axis modes are ignored. More realistic modeling of the microcavity and its coupling to macroscopic light field would lead to quantitative corrections to our results but are not expected to change any conclusions in this paper.

The propagation of the macroscopic light field is governed by the Maxwell equations (with no external "free" charges or currents). The medium outside the cavity is taken as a dielectric with a real refractive index $n_s = \sqrt{\epsilon_s}$ and magnetic permeability $\mu_s = 1$. The oscillator field acts as a local contribution to the polarization density, yielding the following constitutive equations:

$$\mathcal{D}(\mathbf{r},t) = \epsilon_0 n_s^2 \mathcal{E}(\mathbf{r},t) - \hbar t_c \mathbf{E}_{\mathrm{cav}}(x,y,t)\delta(z), \tag{A1}$$

$$\mathcal{H}(\mathbf{r},t) = \frac{1}{\mu_0}\mathcal{B}(\mathbf{r},t). \tag{A2}$$

Here, the functions $\mathcal{E}$, $\mathcal{D}$, $\mathcal{B}$, and $\mathcal{H}$, denote the positive-frequency parts of the respective fields so that, e.g., the (real-valued) electric field is given by $2\mathrm{Re}\mathcal{E}$. $\mathbf{E}_{\mathrm{cav}}(x,y,t)$ is the amplitude of the resonance mode inside the cavity whose equation of motion is given below (and in Ref. 8), and t_c is a parameter characterizing the coupling between the light field and the oscillator mode. Substituting Eqs. (A1) and (A2) into

the Maxwell equations and eliminating $\mathcal{B}$ in the usual way, we obtain a wave equation for the radiation electric field $\mathcal{E}$:

$$\frac{1}{\mu_0}\nabla(\nabla\cdot\mathcal{E})+n_s^2\epsilon_0\frac{\partial^2}{\partial t^2}\mathcal{E}-\frac{1}{\mu_0}\nabla^2\mathcal{E}=\hbar t_c\delta(z)\frac{\partial^2}{\partial t^2}\mathbf{E}_{\rm cav}. \quad \text{(A3)}$$

For near-normal fields, $\nabla\cdot\mathcal{E}\approx 0$ since $\nabla\cdot\mathcal{E}$ is exactly zero at any point outside the cavity, and, across the cavity, it is proportional to the difference in E_z, which is small. We take the approximation $\nabla\cdot\mathcal{E}=0$ in the above equation, and replacing $\epsilon_0\mu_0$ by $1/c^2$, we obtain

$$\frac{n_s^2}{c^2}\frac{\partial^2}{\partial t^2}\mathcal{E}-\nabla^2\mathcal{E}=\frac{\hbar t_c}{\epsilon_0 c^2}\delta(z)\frac{\partial^2}{\partial t^2}\mathbf{E}_{\rm cav}. \quad \text{(A4)}$$

We expand the fields in their spatial Fourier modes in the cavity's plane, i.e., in the (x,y) directions:

$$\mathcal{E}(\mathbf{r},t)=\frac{1}{\mathcal{L}^2}\sum_{\mathbf{k}}e^{i(k_x x+k_y y)}\mathcal{E}_{\mathbf{k}}(z,t), \quad \text{(A5)}$$

$$\mathbf{E}_{\rm cav}(x,y,t)=\frac{1}{\mathcal{L}^2}\sum_{\mathbf{k}}e^{i(k_x x+k_y y)}\mathbf{E}_{{\rm cav},\mathbf{k}}(t), \quad \text{(A6)}$$

where $\mathbf{k}=(k_x,k_y)$ and $\mathcal{L}^2$ is the planar area of the cavity. Substituting into Eq. (A4), we have for each Fourier component:

$$\frac{n_s^2}{c^2}\frac{\partial^2}{\partial t^2}\mathcal{E}_{\mathbf{k}}+\left(k^2-\frac{\partial^2}{\partial z^2}\right)\mathcal{E}_{\mathbf{k}}=\frac{\hbar t_c}{\epsilon_0 c^2}\delta(z)\frac{\partial^2}{\partial t^2}\mathbf{E}_{{\rm cav},\mathbf{k}}, \quad \text{(A7)}$$

where $k^2=k_x^2+k_y^2$. The (positive frequency part of the) general solution of this equation at any point outside of the cavity, $z\neq 0$, is given by

$$\mathcal{E}_{\mathbf{k}}(z,t)=\int_0^\infty\frac{d\omega}{2\pi}[e^{i(k_z(k,\omega)z-\omega t)}\tilde{\mathcal{E}}_{\mathbf{k},+}(\omega) - e^{i(-k_z(k,\omega)z-\omega t)}\tilde{\mathcal{E}}_{\mathbf{k},-}(\omega)], \quad \text{(A8)}$$

where $k_z(k,\omega)=+\sqrt{\frac{\omega^2 n_s^2}{c^2}-k^2}$ and $\tilde{\mathcal{E}}_{\mathbf{k},+}(\omega)$, $\tilde{\mathcal{E}}_{\mathbf{k},-}(\omega)$ are undetermined coefficients. The negative sign in front of the second term is just a convention.

The unique solution under specified initial/boundary conditions are obtained by relating the solutions on the two sides of the cavity. We designate the first integral in Eq. (A8) as the right-going field $\mathcal{E}_{\mathbf{k},+}(z,t)$ and the second integral as the left-going field $\mathcal{E}_{\mathbf{k},-}(z,t)$. We also put in labels to indicate the domain of the fields: $\mathcal{E}^R_{\mathbf{k},+}(z,t)$, $\mathcal{E}^R_{\mathbf{k},-}(z,t)$, $\tilde{\mathcal{E}}^R_{\mathbf{k},+}(\omega)$, $\tilde{\mathcal{E}}^R_{\mathbf{k},-}(\omega)$ are the fields and coefficients on the right side of the cavity, i.e., for $z>0$, and $\mathcal{E}^L_{\mathbf{k},+}(z,t)$, $\mathcal{E}^L_{\mathbf{k},-}(z,t)$, $\tilde{\mathcal{E}}^L_{\mathbf{k},+}(\omega)$, $\tilde{\mathcal{E}}^L_{\mathbf{k},-}(\omega)$ are the fields and coefficients on the left side of the cavity, i.e., for $z<0$. We also decompose the oscillator field as

$$\mathbf{E}_{{\rm cav},\mathbf{k}}(t)=\int_0^\infty\frac{d\omega}{2\pi}e^{-i\omega t}\tilde{\mathbf{E}}_{{\rm cav},\mathbf{k}}(\omega). \quad \text{(A9)}$$

The solution fields on the two sides of the cavity are related by noting that Eq. (A7) implies continuity of $\mathcal{E}_{\mathbf{k}}(z,t)$ at $z=0$:

$$\mathcal{E}^R_{\mathbf{k},+}(0,t)-\mathcal{E}^R_{\mathbf{k},-}(0,t)=\mathcal{E}^L_{\mathbf{k},+}(0,t)-\mathcal{E}^L_{\mathbf{k},-}(0,t), \quad \text{(A10)}$$

and a finite jump of $\frac{\partial}{\partial z}\mathcal{E}_{\mathbf{k}}(z,t)$ across $z=0$:

$$\frac{\partial}{\partial z}\left[\mathcal{E}^R_{\mathbf{k},+}(z,t)-\mathcal{E}^R_{\mathbf{k},-}(z,t)\right]_{z=0_+}-\frac{\partial}{\partial z}\left[\mathcal{E}^L_{\mathbf{k},+}(z,t)-\mathcal{E}^L_{\mathbf{k},-}(z,t)\right]_{z=0_-} = -\frac{\hbar t_c}{\epsilon_0 c^2}\frac{\partial^2}{\partial t^2}\mathbf{E}_{{\rm cav},\mathbf{k}}(t). \quad \text{(A11)}$$

Using the expansions Eqs. (A8) and (A9), we get the following for each frequency component:

$$\tilde{\mathcal{E}}^R_{\mathbf{k},+}(\omega)+\tilde{\mathcal{E}}^R_{\mathbf{k},-}(\omega)-\tilde{\mathcal{E}}^L_{\mathbf{k},+}(\omega)-\tilde{\mathcal{E}}^L_{\mathbf{k},-}(\omega)=-i\frac{\hbar t_c\omega^2}{\epsilon_0 c^2 k_z}\tilde{\mathbf{E}}_{{\rm cav},\mathbf{k}}(\omega). \quad \text{(A12)}$$

We again invoke the approximation $k^2\approx 0\Rightarrow k_z\approx\omega n_s/c$ on the right-hand side of Eq. (A12), which becomes $\frac{\hbar t_c}{\epsilon_0 c n_s}[-i\omega\tilde{\mathbf{E}}_{{\rm cav},\mathbf{k}}(\omega)]$. Taking the inverse Fourier transform back to the time domain, we get

$$\mathcal{E}^R_{\mathbf{k},+}(0,t)+\mathcal{E}^R_{\mathbf{k},-}(0,t)-\mathcal{E}^L_{\mathbf{k},+}(0,t)-\mathcal{E}^L_{\mathbf{k},-}(0,t) = \frac{\hbar t_c}{\epsilon_0 c n_s}\frac{\partial}{\partial t}\mathbf{E}_{{\rm cav},\mathbf{k}}(t). \quad \text{(A13)}$$

Equations (A10) and (A13) provide two conditions which allow to express the fields on one side of the cavity in terms of those on the other side. The result is

$$\begin{pmatrix}\mathcal{E}^{\mathbf{R}}_{\mathbf{k},+}(0,t)\\ \mathcal{E}^R_{\mathbf{k},-}(0,t)\end{pmatrix}=\begin{pmatrix}\mathcal{E}^{\mathbf{L}}_{\mathbf{k},+}(0,t)\\ \mathcal{E}^L_{\mathbf{k},-}(0,t)\end{pmatrix}+\frac{\hbar t_c}{2\epsilon_0 c n_s}\frac{\partial}{\partial t}\mathbf{E}_{{\rm cav},\mathbf{k}}(t)\begin{pmatrix}1\\1\end{pmatrix}. \quad \text{(A14)}$$

In our setting, all the fields have the same circular polarization, say +. The (+)-polarization vectors for all the slightly obliquely directed beams are of course not exactly parallel to each other, but consistent with the small-k approximations we have made, so far, we ignore these slight misalignments and use a common unit vector $\hat{\mathbf{e}}_+=(\hat{x}+i\hat{y})/\sqrt{2}$. Then, using the notations in Ref. 8, we write $\mathcal{E}^L_{\mathbf{k},+}(0,t)=\mathcal{L}^2E_{\mathbf{k},{\rm inc}}(t)\hat{\mathbf{e}}_+$, $\mathcal{E}^L_{\mathbf{k},-}(0,t)=\mathcal{L}^2E_{\mathbf{k},{\rm refl}}(t)\hat{\mathbf{e}}_+$, $\mathcal{E}^R_{\mathbf{k},+}(0,t)=\mathcal{L}^2E_{\mathbf{k},{\rm trans}}(t)\hat{\mathbf{e}}_+$, $\mathcal{E}^R_{\mathbf{k},-}(0,t)=0$, and $\mathbf{E}_{{\rm cav},\mathbf{k}}(t)=\mathcal{L}^2E_{\mathbf{k}}(t)\hat{\mathbf{e}}_+$. [We reiterate that $E_{\mathbf{k}}(t)$ denotes the cavity oscillator field and is not to be confused with $\mathcal{E}_{\mathbf{k}}(t)$, which denotes an macroscopic field mode.] From Eq. (A14), we obtain

$$E_{\mathbf{k},{\rm trans}}(t)=E_{\mathbf{k},{\rm inc}}(t)-E_{\mathbf{k},{\rm refl}}(t), \quad \text{(A15)}$$

$$E_{\mathbf{k},{\rm refl}}(t)=-\frac{\hbar t_c}{2\epsilon_0 c n_s}\frac{\partial}{\partial t}E_{\mathbf{k}}(t). \quad \text{(A16)}$$

It is also clear that $E_{\mathbf{k},{\rm trans}}(t)$ is the radiation field at the position of the cavity and thus is equal to the driving radiation field in the equation for $E_{\mathbf{k}}(t)$ [see Eq. (7)]: $E^{\rm eff}_{\mathbf{k},{\rm inc}}=E_{\mathbf{k},{\rm trans}}(t)$.

In the remainder of this appendix, we show that the postulated equation of motion for the cavity field $E_{\mathbf{k}}(t)$, Eq. (7), leads, in conjunction with the equations for the macroscopic field and the QW exciton field, naturally to the interpretation of $|E_{\mathbf{k}}(t)|^2$ as the number of photons in mode $\mathbf{k}$ per unit area. Our argument is based on considering the energy balance in our theory. From the Maxwell equations and the constitutive equations Eqs. (A1) and (A2), we obtain in the usual way the continuity equation for the macroscopic field's energy flux:

$$\frac{\partial}{\partial t}u_{\rm em}+\nabla\cdot\mathbf{S}=+2\hbar t_c\delta(z){\rm Re}\left(\mathcal{E}^*\cdot\frac{\partial}{\partial t}\mathbf{E}_{\rm cav}\right), \quad \text{(A17)}$$

where

$$u_{\rm em}=n_s^2\epsilon_0\mathcal{E}^*\cdot\mathcal{E}+\frac{1}{\mu_0}\mathcal{B}^*\cdot\mathcal{B}, \quad \text{(A18)}$$

$$\mathbf{S}=2{\rm Re}\left(\mathcal{E}^*\times\frac{1}{\mu_0}\mathcal{B}\right). \quad \text{(A19)}$$

$u_{\rm em}$ is the averaged light field energy density, including the energy of interaction with the background dielectric, and **S**, the Poynting vector, is the averaged energy flux density. Integrating over an infinitesimal interval across the cavity at $z = 0$ gives

$$\hat{z}\cdot\left[2\mathrm{Re}\left(\mathcal{E}^*\times\frac{1}{\mu_0}\mathcal{B}\right)_{z=0_+}-2\mathrm{Re}\left(\mathcal{E}^*\times\frac{1}{\mu_0}\mathcal{B}\right)_{z=0_-}\right]$$
$$=\hbar t_c 2\mathrm{Re}\left[\mathcal{E}^*(z=0)\cdot\frac{\partial}{\partial t}\mathbf{E}_{\rm cav}\right]. \quad \text{(A20)}$$

Since the left-hand side of Eq. (A20) is the net field energy flux density coming out of the cavity, the right-hand side should be interpreted as the negative of the rate of energy change per unit area inside the cavity. If we integrate the right-hand side over the cavity's plane and specialize to our setting, we get

$$\hbar t_c\int dxdy 2\mathrm{Re}\left[\mathcal{E}^*(z=0)\cdot\frac{\partial}{\partial t}\mathbf{E}_{\rm cav}\right]$$
$$=\frac{\hbar t_c}{\mathcal{L}^2}\sum_{\mathbf{k}}2\mathrm{Re}\left[\mathcal{E}^*_{\mathbf{k}}(0,t)\cdot\frac{\partial}{\partial t}\mathbf{E}_{\mathrm{cav},\mathbf{k}}\right]$$
$$=\hbar t_c\mathcal{L}^2\sum_{\mathbf{k}}2\mathrm{Re}\left(E^*_{\mathbf{k},\mathrm{trans}}\frac{\partial}{\partial t}E_{\mathbf{k}}\right). \quad \text{(A21)}$$

We now use the equation of motion of $E_{\mathbf{k}}(t)$, Eq. (7), to eliminate $E^*_{\mathbf{k},\mathrm{trans}}$, and we get for the right-hand side of Eq. (A21):

$$-\mathcal{L}^2\sum_{\mathbf{k}}\left[\hbar\omega^c_{\mathbf{k}}\frac{\partial}{\partial t}|E_{\mathbf{k}}|^2-2\mathrm{Re}\left(\Omega_{\mathbf{k}}p^*_{\mathbf{k}}\frac{\partial}{\partial t}E_{\mathbf{k}}\right)\right], \quad \text{(A22)}$$

$\Omega_{\mathbf{k}}$ being real. From the first term, one can see that $|E_{\mathbf{k}}|^2$ is to be interpreted as the number of photons per unit area in the cavity mode **k**. The second term represents an energy exchange with the exciton field. We can cast it into a more physically meaningful form by using $p_{\mathbf{k}}$'s equation of motion. For simplicity, we illustrate this point with the linearized form of Eq. (10). We first write the term in question as

$$-2\mathrm{Re}\left(\Omega_{\mathbf{k}}p^*_{\mathbf{k}}\frac{\partial}{\partial t}E_{\mathbf{k}}\right)=-\frac{\partial}{\partial t}2\mathrm{Re}(\Omega_{\mathbf{k}}p^*_{\mathbf{k}}E_{\mathbf{k}})$$
$$+2\mathrm{Re}\left(\Omega_{\mathbf{k}}E_{\mathbf{k}}\frac{\partial}{\partial t}p^*_{\mathbf{k}}\right). \quad \text{(A23)}$$

For the second term, we eliminate $E_{\mathbf{k}}$ using Eq. (10) without the nonlinear terms and finally obtain for Eq. (A22),

$$-\mathcal{L}^2\sum_{\mathbf{k}}\left\{\frac{\partial}{\partial t}\left[\begin{pmatrix}E^*_{\mathbf{k}} & p^*_{\mathbf{k}}\end{pmatrix}\begin{pmatrix}\hbar\omega^c_{\mathbf{k}} & -\Omega_{\mathbf{k}}\\ -\Omega_{\mathbf{k}} & \varepsilon^x_{\mathbf{k}}\end{pmatrix}\begin{pmatrix}E_{\mathbf{k}}\\ p_{\mathbf{k}}\end{pmatrix}\right]\right.$$
$$\left.+2\gamma_x\mathrm{Im}\left(p_{\mathbf{k}}\frac{\partial}{\partial t}p^*_{\mathbf{k}}\right)\right\}. \quad \text{(A24)}$$

The first term is the rate of change of energy of the *linear* polariton field inside the cavity, and the second term is the rate of energy loss by dissipation.

We can also reduce the left hand side of Eq. (A20) to our case where all fields are in the same circular polarization (spin) state. We state the result here:

$$\frac{c}{n_s}\mathcal{L}^2\sum_{\mathbf{k}}2n_s^2\epsilon_0[|E_{\mathbf{k},\mathrm{trans}}(t)|^2+|E_{\mathbf{k},\mathrm{refl}}(t)|^2-|E_{\mathbf{k},\mathrm{inc}}(t)|^2]. \quad \text{(A25)}$$

It is of course also simple to verify the equality between Eqs. (A25) and (A22) by directly applying Eqs. (5)–(8).

*kwong@optics.arizona.edu

[1] A. Yariv and D. M. Pepper, Opt. Lett. **1**, 16 (1977).
[2] G. Grynberg and J. Paye, Europhys. Lett. **8**, 29 (1989).
[3] G. D'Alessandro and W. J. Firth, Phys. Rev. Lett. **66**, 2597 (1991).
[4] J. B. Geddes, R. A. Indik, J. V. Moloney, and W. J. Firth, Phys. Rev. A **50**, 3471 (1994).
[5] J. Lega, J. V. Moloney, and A. C. Newell, Physica D **83**, 478 (1995).
[6] L. A. Lugiato, L. Spinelli, G. Tissoni, and M. Brambilla, J. Opt. B **1**, 43 (1999).
[7] R. Kheradmand, M. Sahrai, H. Tajalli, G. Tissoni, and L. A. Lugiato, Eur. Phys. J. D **47**, 107 (2008).
[8] S. Schumacher, N. Kwong, R. Binder, and A. Smirl, Phys. Status Solidi Rapid Res. Lett. **3**, 10 (2009).
[9] S. P. Hegarty, G. Huyet, J. G. McInerney, and K. D. Choquette, Phys. Rev. Lett. **82**, 1434 (1999).
[10] J. Houlthan, J. R. O'Callaghan, V. Voignier, G. Huyut, J. G. McInerney, and B. Corbett, Opt. Lett. **26**, 1556 (2001).
[11] G. Grynberg, E. L. Bihan, P. Verkerk, P. Simoneau, J. R. R. Leite, D. Bloch, S. L. Boiteux, and M. Ducloy, Opt. Comm. **67**, 363 (1988).
[12] G. Giusfredi, J. F. Valley, R. Pon, G. Khitrova, and H. M. Gibbs, J. Opt. Soc. Am. B **5**, 1181 (1988).
[13] R. Herrero, E. GrosseWesthoff, A. Aumann, T. Ackemann, Y. A. Logvin, and W. Lange, Phys. Rev. Lett. **82**, 4627 (1999).
[14] A. M. C. Dawes, L. Illing, S. M. Clark, and D. J. Gauthier, Science **308**, 672 (2005).
[15] E. Benkler, M. Kreuzer, R. Neubecker, and T. Tschudi, Phys. Rev. Lett. **84**, 879 (2000).
[16] C. Denz, M. Schwab, M. Sedlatschek, T. Tschudi, and T. Honda, J. Opt. Soc. Am. B **15**, 2057 (1998).
[17] V. Ardizzone, P. Lewandowski, Y. C. Tse, N. H. Kwong, M. H. Luk, A. Lücke, M. Abbarchi, E. Baudin, E. Galopin, J. Bloch, A. Lemaitre, P. T. Leung, P. Roussignol, R. Binder, J. Tignon, and S. Schumacher (unpublished).
[18] N. B. Abraham and W. J. Firth, J. Opt. Soc. Am. B **7**, 951 (1990).
[19] L. A. Lugiato, Chaos Solitons Fractals **4**, 1251 (1994).
[20] K. Staliūnas and V. J. Sánchez-Morcillo, *Transverse Patterns in Nonlinear Optical Resonators* (Springer, Berlin, 2003).
[21] M. C. Cross and P. C. Hohenberg, Rev. Mod. Phys. **65**, 851 (1993).
[22] A. C. Newell, T. Passot, and J. Lega, Annu. Rev. Fluid Mech. **25**, 399 (1993).
[23] A. M. C. Dawes, D. J. Gauthier, S. Schumacher, N. H. Kwong, R. Binder, and A. L. Smirl, Laser Photonics Rev. **4**, 221 (2010).

[24]P. G. Savvidis, J. J. Baumberg, R. M. Stevenson, M. S. Skolnick, D. M. Whittaker, and J. S. Roberts, Phys. Rev. Lett. **84**, 1547 (2000).
[25]R. Huang, F. Tassone, and Y. Yamamoto, Phys. Rev. B **61**, R7854 (2000).
[26]S. Savasta, O. Di Stefano, and R. Girlanda, Phys. Rev. Lett. **90**, 096403 (2003).
[27]N. H. Kwong, R. Takayama, I. Rumyantsev, M. Kuwata-Gonokami, and R. Binder, Phys. Rev. B **64**, 045316 (2001).
[28]R. Takayama, N. H. Kwong, I. Rumyantsev, M. Kuwata-Gonokami, and R. Binder, Eur. Phys. J. B **25**, 445 (2002).
[29]C. Ciuti, P. Schwendimann, B. Deveaud, and A. Quattropani, Phys. Rev. B **62**, R4825 (2000).
[30]D. M. Whittaker, Phys. Rev. B **63**, 193305 (2001).
[31]See, for example, *Exciton Polaritons in Microcavities*, edited by D. Sanvitto and V. Timofeev (Springer, Berlin, 2012).
[32]A. Amo, S. Pigeon, D. Sanvitto, V. G. Sala, R. Hivet, I. Carusotto, F. Pisanello, G. Lemenager, R. Houdre, E. Giacobino, C. Ciuti, and A. Bramati, Science **332**, 1167 (2011).
[33]G. Tosi, G. Christmann, N. G. Berloff, P. Tsotsis, T. Gao, Z. Hatzopoulos, P. G. Savvidis, and J. J. Baumberg, Nat. Commun. **3**, 1243 (2012).
[34]R. M. Stevenson, V. N. Astratov, M. S. Skolnick, D. M. Whittaker, M. Emam-Ismail, A. I. Tartakovskii, P. G. Savvidis, J. J. Baumberg, and J. S. Roberts, Phys. Rev. Lett. **85**, 3680 (2000).
[35]M. Romanelli, C. Leyder, J. Ph. Karr, E. Giacobino, and A. Bramati, Phys. Rev. Lett. **98**, 106401 (2007).
[36]D. Ballarini, D. Sanvitto, A. Amo, L. Vina, M. Wouters, I. Carusotto, A. Lemaitre, and J. Bloch, Phys. Rev. Lett. **102**, 056402 (2009).
[37]S. Schumacher, N. H. Kwong, and R. Binder, Phys. Rev. B **76**, 245324 (2007).
[38]W. Schäfer and M. Wegener, *Semiconductor Optics and Transport Phenomena* (Springer, Berlin, 2002).
[39]N. H. Kwong and R. Binder, Phys. Rev. B **61**, 8341 (2000).
[40]Z. S. Yang, N. H. Kwong, R. Binder, and A. L. Smirl, J. Opt. Soc. B **22**, 2144 (2005).
[41]T. Stroucken, A. Knorr, P. Thomas, and S. W. Koch, Phys. Rev. B **53**, 2026 (1996).
[42]J. Kim, E. Malic, M. Richter, A. Wilms, and A. Knorr, IEEE J. Quantum Electron. **46**, 1115 (2010).
[43]V. M. Axt and A. Stahl, Z. Phys. B **93**, 195 (1994).
[44]M. H. Luk, Master's thesis, Chinese University of Hong Kong, 2012.
[45]M. Abbarchi, C. Diederichs, L. Largeau, V. Ardizzone, O. Mauguin, T. Lecomte, A. Lemaitre, J. Bloch, P. Roussignol, and J. Tignon, Phys. Rev. B **85**, 045316 (2012).
[46]O. A. Egorov, D. V. Skryabin, and F. Lederer, Phys. Rev. B **84**, 165305 (2011).
[47]W. E. Lamb, Phys. Rev. **134**, A1429 (1964).
[48]S. Ciliberto, P. Coullet, J. Lega, E. Pampaloni, and C. Perez-Garcia, Phys. Rev. Lett. **65**, 2370 (1990).
[49]S. Longhi and A. Geraci, Phys. Rev. A **57**, R2281 (1998).
[50]E. Runge and R. Zimmermann, Phys. Stat. Sol. (b) **221**, 269 (2000).
[51]F. Marchetti, J. Keeling, M. Szymanska, and P. Littlewood, Phys. Rev. Lett. **96**, 066405 (2006).
[52]I. Carusotto and C. Ciuti, Phys. Rev. Lett. **93**, 166401 (2004).
[53]W. Langbein and J. M. Hvam, Phys. Rev. Lett. **88**, 047401 (2002).